

Radiation hydrodynamics simulations of the formation of direct-collapse supermassive stellar systems

Sunmyon Chon,^{1†} Takashi Hosokawa,² and Naoki Yoshida,¹³

¹*Department of Physics, School of Science, University of Tokyo, Bunkyo, Tokyo 113-0033, Japan*

²*Department of Physics, Kyoto University, Kyoto 606-8502, Japan*

³*Kavli Institute for the Physics and Mathematics of the Universe (WPI), Todai Institutes for Advanced Study*

Accepted XXX. Received YYY; in original form ZZZ

ABSTRACT

Formation of supermassive stars (SMSs) with mass $\gtrsim 10^4 M_\odot$ is a promising pathway to seed the formation of supermassive black holes in the early universe. The so-called direct-collapse (DC) model postulates that such an SMS forms in a hot gas cloud irradiated by a nearby star-forming galaxy. We study the DC SMS formation in a fully cosmological context using three-dimensional radiation hydrodynamics simulations. We initialize our simulations using the outputs of the cosmological simulation of Chon et al. (2016), where two DC gas clouds are identified. The long-term evolution over a hundred thousand years is followed from the formation of embryo protostars through their growth to SMSs. We show that the strength of the tidal force by a nearby galaxy determines the multiplicity of the formed stars and affects the protostellar growth. In one case, where a collapsing cloud is significantly stretched by strong tidal force, multiple star-disk systems are formed via filament fragmentation. Small-scale fragmentation occurs in each circumstellar disk, and more than 10 stars with masses of a few $\times 10^3 M_\odot$ are finally formed. Interestingly, about a half of them are found as massive binary stars. In the other case, the gas cloud collapses nearly spherically under a relatively weak tidal field, and a single star-disk system is formed. Only a few SMSs with masses $\sim 10^4 M_\odot$ are found already after evolution of a hundred thousand years, and the SMSs are expected to grow further by gas accretion and to leave massive blackholes at the end of their lives.

1 INTRODUCTION

Recent wide-field surveys discovered that a population of supermassive black holes (SMBHs) already existed at redshift $z \gtrsim 6$ (Willott et al. 2010; Mortlock et al. 2011; Wu et al. 2015; Venemans et al. 2016). Since the cosmic age at $z \simeq 6$ is about 0.8 Gyr, the fact poses a challenge to the theory of SMBH formation. One naive solution would be efficient growth of a seed BH with $\sim 10^2 M_\odot$ by gas accretion over several hundred millions years, to attain barely the observationally inferred mass $\gtrsim 10^9 M_\odot$ of the early SMBHs. Obviously, the seed BH mass needs to be sufficiently large, but observationally confirmed stellar-mass BHs via X-ray or gravitational wave (GW) emissions do not have masses as large as $100 M_\odot$ (e.g. Casares & Jonker 2014; Abbott et al. 2016). Recent numerical simulations suggest that the mass distribution of Population III (Pop III) stars can extend to $\sim 100 M_\odot$ (e.g. McKee & Tan 2008; Hosokawa et al. 2011, 2016; Susa et al. 2014; Hirano et al. 2014, 2015) and the most massive population leave equally massive BHs (e.g. Heger et al. 2003). The remnant BHs may grow into SMBHs exceeding $10^9 M_\odot$ by $z \gtrsim 6$, if efficient accretion with a near-Eddington rate, is maintained for about a billion years (e.g. Li et al. 2007). However, it is already known that radiation feedback effects from both the stars and accreting

BHs reduce the accretion rate far below the Eddington value (e.g. Yoshida 2006; Milosavljević et al. 2009; Park & Ricotti 2011).

Supermassive stars (SMSs) with $\gtrsim 10^5 M_\odot$ are thought to collapse via general relativistic instability (e.g. Shibata & Shapiro 2002; Umeda et al. 2016) to become massive BHs, and hence may be promising “seeds” for the formation of early SMBHs (Bromm & Loeb 2003; Hirano et al. 2017). Cosmological simulations suggest that the remnant BHs of early SMSs can grow into SMBHs exceeding $10^9 M_\odot$ in several hundred millions years via further mass accretion, and also by circumventing the stellar feedback effects (e.g., Di Matteo et al. 2012; Volonteri 2010).

There are a few formation pathways of SMSs including the formation under supersonic gas streams (e.g. Hirano et al. 2017) and a popular ultra-violet (UV) radiation driven collapse (Chon et al. 2016; Regan et al. 2017). For the latter, consider that the Lyman-Werner (LW; $11.2 \text{ eV} \leq h\nu \leq 13.6 \text{ eV}$) radiation emitted by nearby galaxies is strong enough to destroy H_2 molecules in the cloud via photodissociation. If such a cloud is hosted by a massive dark halo with $T_{\text{vir}} \gtrsim 8000 \text{ K}$ (the so-called atomic-cooling halo), the cloud collapses isothermally at $T \simeq 8000 \text{ K}$ via atomic hydrogen cooling. Such a high temperature gas collapse induces rapid mass accretion onto a protostar with a large

rate of $\dot{M} \gtrsim 0.1 M_{\odot} \text{ yr}^{-1}$ (e.g. [Latif et al. 2013](#)). If the fast accretion continues, the stellar mass reaches $10^5 M_{\odot}$ within its lifetime of about a few million years.

The LW radiation intensity, usually normalized in units of $10^{-21} \text{ erg s}^{-1} \text{ Hz}^{-1} \text{ cm}^{-2} \text{ str}^{-1}$ (J_{21}), is a key parameter to set the conditions for the so-called direct collapse (DC) of a primordial gas. Various authors have investigated the critical J_{21} for DC. Recent studies suggest that $J_{21} \gtrsim 10^2\text{--}10^3$ is at least necessary (e.g. [Omukai 2001](#); [Shang et al. 2010](#); [Latif et al. 2014](#); [Sugimura et al. 2014](#)). The number density of the DCBHs has been also estimated by various authors (e.g. [Agarwal et al. 2012](#); [Dijkstra et al. 2014](#); [Habouzit et al. 2016](#)). They use galaxy formation models to investigate the distribution of J_{21} at the locations of atomic-cooling halos and count the number density of the DC candidate halos in a volume of $\sim \text{Mpc}^{-3} - \text{Gpc}^{-3}$. These previous studies, however, assume that all the halos that satisfy a few DC conditions can actually bear SMSs. It remains unclear if the gas cloud in the DC halos can actually collapse and produce SMSs.

Earlier in [Chon et al. \(2016\)](#), we performed cosmological hydrodynamics simulations of the formation of DC gas clouds. We first used a semi-analytic model of early galaxy formation and traced the star formation history of each halo to determine accurately the radiation intensity J_{21} at the positions of neighboring atomic-cooling halos. We then performed hydrodynamics simulations and found that a large fraction of DC clouds do *not* collapse, because of disruption by the strong tidal force exerted by the nearby galaxy. Only 2 out of the 42 examined cases are successful in terms of DC. The remaining important question is whether or not SMSs are formed in the ‘successful’ cases. We follow the subsequent protostellar accretion evolution in the present paper.

The final mass of an SMS is determined through dynamical interplay between the central protostar(s), the circumstellar disk, and the infalling gas, where gravitational fragmentation may occur. Recent high resolution simulations show no significant fragmentation during the early collapse phase of a DC cloud ([Bromm & Loeb 2003](#); [Regan & Haehnelt 2009](#); [Latif et al. 2013](#); [Inayoshi et al. 2014](#); [Choi et al. 2015](#)). In the later accretion phase after the birth of a protostar, however, the circumstellar disk grows in mass and becomes gravitationally unstable to trigger disk fragmentation (e.g., [Becerra et al. 2015](#); [Sakurai et al. 2016](#)), possibly leading to formation of a star cluster, rather than the formation of a single SMS.

Radiative feedback from an accreting protostar is another key process, which can limit the stellar mass growth by halting the accretion (e.g. [McKee & Tan 2008](#); [Hosokawa et al. 2011](#)). Since the structure of an accreting protostar under rapid accretion of $\gtrsim 0.1 M_{\odot} \text{ yr}^{-1}$ is very different from that of a main-sequence star, with a very bloated envelope, the UV feedback is thought to be weak for the DC case ([Hosokawa et al. 2012, 2013](#); [Schleicher et al. 2013](#)). Its effective temperature is only $T_{\text{eff}} \simeq 5000 \text{ K}$, with which the stellar UV emissivity remains small even when the stellar mass reaches $\sim 10^4\text{--}10^5 M_{\odot}$. The UV feedback strength is intrinsically coupled to the fragmentation described above because individual protostars begin to contract if the accretion rate falls below $\sim 10^{-2} M_{\odot} \text{ yr}^{-1}$.

In this work, we study the protostellar evolution in the later accretion phase in the DC model. We start our ra-

diation hydrodynamic simulations from the final snapshots of the two collapsing clouds found in [Chon et al. \(2016\)](#), and follow the subsequent evolution for $\sim 0.1 \text{ Myrs}$. We show that the tidal force exerted on the clouds critically affects the stellar mass growth. In one case, strong tidal field distorts the cloud and induces large-scale filament fragmentation. The typical stellar mass is found to be as small as a few $\times 10^3 M_{\odot}$. The other cloud experiences relatively weak tidal force, and stars with mass greater than $10^4 M_{\odot}$ are actually formed within 0.1 Myrs . The latter case is a promising SMS formation process, whereas an interesting end-product of the former case is massive star binaries. Both have important implications for direct and indirect observations.

The rest of this paper is organized as follows. In Section 2, we describe our numerical methods, setup, and initial condition. In Section 3, we present the early evolution of the cloud collapse until the central density reaches 10^{13} cm^{-3} , and then describe the evolution in the later protostellar accretion stage for the duration of 0.1 Myr . In Section 4, we investigate the role of the UV feedback in our simulations. The physical effects not included in our study are discussed in Section 5. Finally, we summarize our results in Section 6.

2 METHODOLOGY

We use the N-body + Smoothed Particle Hydrodynamics code **Gadget2** ([Springel 2005](#)) with the following extensions. We implement sink particles to follow the protostar evolution. We use a stellar evolution model to follow the radii (structure) and the luminosities of accreting protostars. Finally, we implement a ray tracing method to follow the radiation feedback from accreting protostars. In this section, we describe our numerical method.

2.1 Initial conditions

[Chon et al. \(2016\)](#) find that only 2 clouds collapse with the gas density reaching 10^8 cm^{-3} . The clouds are assembled rapidly through mergers, and gravitational collapse is triggered when their masses exceed a critical mass for DC. Fig. 1 summarizes the characteristics of these two clouds. We label them as “filamentary” and “spherical” clouds. The filamentary cloud is located close to the center of a massive galaxy with the separation of $\sim 100 \text{ pc}$. The nearby galaxy has a mass of $10^{10} M_{\odot}$, which tidally distorts and elongates the collapsing gas cloud (left top panel in Fig. 1). The spherical cloud is located far from a massive galaxy with the separation of $\sim 5 \text{ kpc}$ (right bottom panel in Fig. 1). The LW radiation is mainly provided by less massive galaxy with a mass of $\sim 10^7 M_{\odot}$ at $\sim 400 \text{ pc}$ from the spherical cloud. Thus the cloud can avoid the tidal deformation from the main galaxy and is able to collapse almost spherically ([Visbal et al. 2014](#)).

To reduce the computational costs, we extract the region around the collapsing cloud center when the central gas density has reached 10^8 cm^{-3} . The extracted region has the radial extension of ~ 10 and 100 pc from the cloud center for gas and dark matter particles, respectively. We include the DM particles in larger region than the gas particles, since the tidal field from the nearby massive galaxy can be

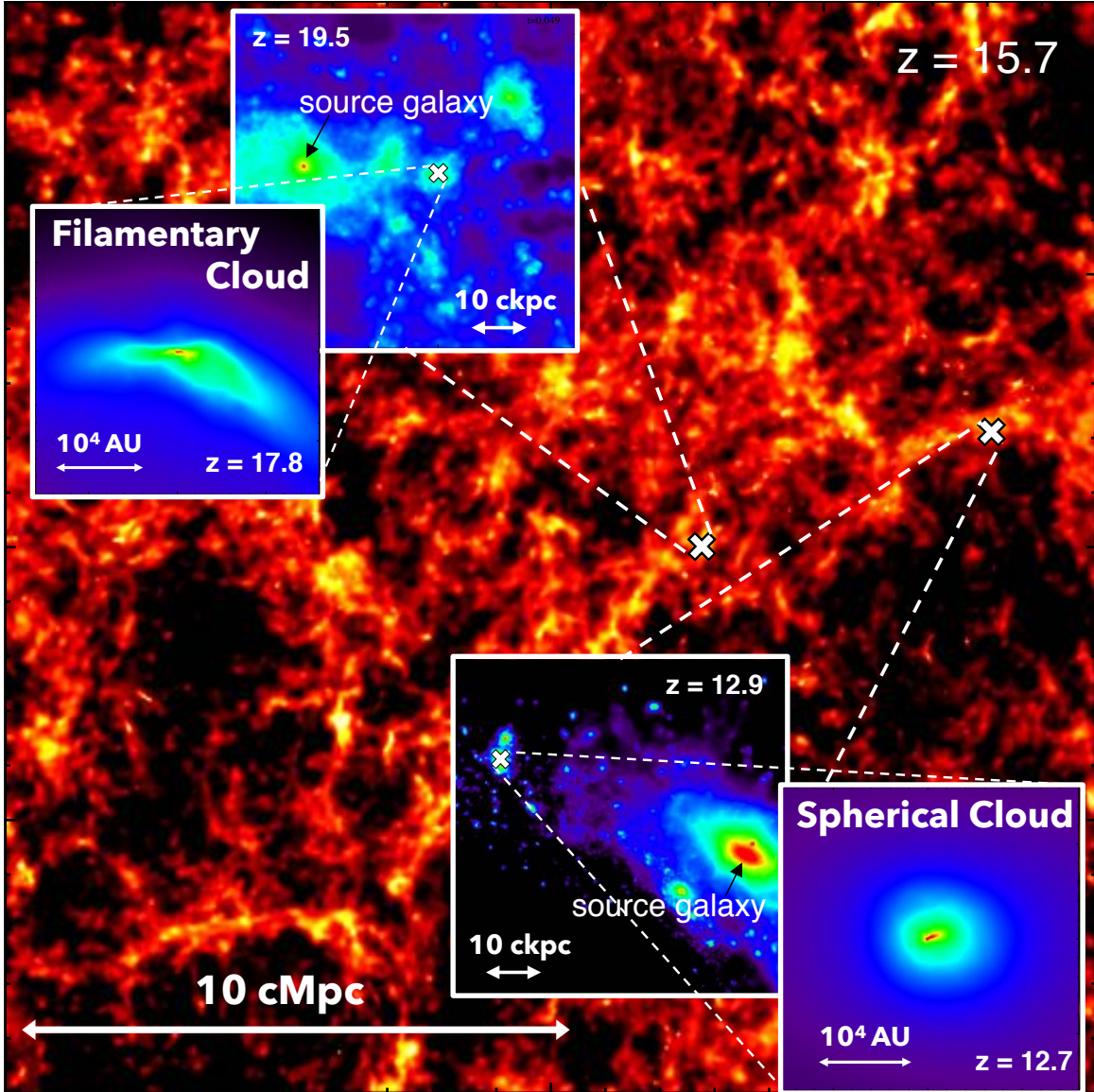


Figure 1. Schematic view showing the locations of the spherical and the filamentary clouds. The clouds are taken from a large-scale cosmological simulation with the box size of $20 h^{-1}\text{Mpc}$ on a side. In our previous study [Chon et al. \(2016\)](#), the cloud evolution has been followed until the central density reaches 10^8 cm^{-3} during the early run-away collapse. We further follow the subsequent long-term evolution of the protostellar accretion for $\sim 0.1 \text{ Myr}$ in this paper.

also important in the later accretion phase of the collapsing clouds.

2.2 Chemistry

We include 9 primordial species (e^- , H , H^+ , He , He^+ , He^{2+} , H_2 , H_2^+ , and H^-) and solve the chemical reaction and the energy equation considering cooling process ([Yoshida et al. 2003](#)). Here, we omit the HD chemistry because the cloud temperature is so high that the abundance of species including deuterium is negligible.

We include an external radiation field which dissociates H_2 and H^- . The external LW intensity is set to be the value obtained by our semi-analytic calculation in [Chon et al. \(2016\)](#). The intensities are 5000 (filamentary) and

1000 (spherical cloud) in units of J_{21} and almost constant throughout the calculation. We assume that the radiation spectrum is described by a 10^4 K black body as in [Chon et al. \(2016\)](#). We do not consider attenuation of LW radiation by the gas self-shielding since H_2 is mainly dissociated by the collision with H atom (Section 5.3). We do not consider the ionizing radiation from the nearby massive galaxy since it is attenuated by the intergalactic matter and by the cloud envelope ([Chon & Latif 2017](#)).

Once protostars are formed, we also consider the local radiation feedback originating from them. We implement only the local ionizing radiation which ionizes hydrogen atoms by using a ray-tracing scheme (Section 2.5). The local LW radiation is not included in our calculations for the following two reasons; the intensity of the local LW radia-

tion is smaller than or comparable to the external one, and the H_2 dissociation rate by LW radiation is smaller than that by the collisional dissociation with H atom in a hot gas (Inayoshi & Omukai 2012). Thus, we expect the local LW radiation from accreting protostars does not affect the thermal evolution of the collapsing clouds that are already exposed to a strong external LW radiation.

We adopt an optically-thin $\text{Ly}\alpha$ cooling rate throughout the calculation, even at densities greater than $\sim 10^4 \text{ cm}^{-3}$ where the gas actually becomes optically thick to $\text{Ly}\alpha$ photons. In practice, this prescription regulates the cloud temperature at $\sim 8000 \text{ K}$, which resembles the realistic temperature evolution that considers other H-cooling processes (e.g. 3p-2s transition, H^- continuum, see Becerra et al. 2015).

Since we are interested in the stellar evolution for a long period of $\sim 0.1\text{--}1 \text{ Myr}$, we use a ‘hard’ adiabatic equation state with $\gamma = 5/3$ when the gas density exceeds $n_{\text{adib}} = 10^{13} \text{ cm}^{-3}$. Otherwise, the increased gas density makes the time step too short and the system’s long-term evolution cannot be followed. To see how this adiabatic prescription affects our results, we run test calculations with changing n_{adib} (see Section 5.4 for details). In short, binaries with the smaller separations appear using the smaller threshold density. In our cases, however, the stellar radius becomes comparable to such a small separation with very rapid accretion (see Section 2.5). The binaries with separations of $< 100 \text{ AU}$ are merging away, and they do not survive in our simulations anyway.

2.3 Particle splitting

It is necessary to resolve the local Jeans length (e.g. Truelove et al. 1997; Nelson 2006). We split a gas particle into 13 daughter particles following Kitsionas & Whitworth (2002), when its density reaches $n = 10^8$ and 10^{10} cm^{-3} . The initial mass of the gas particle is $1.6 M_\odot$ and the gas particle mass with $n > 10^{10} \text{ cm}^{-3}$ is $9.4 \times 10^{-3} M_\odot$. This prescription allows us to resolve the Jeans length by more than ten times the smoothing length of a gas particle (e.g. Stacy et al. 2016).

2.4 Sink particles

We implement a sink particle technique to emulate accreting protostars in a gas cloud. We generate a sink particle when the local gas density exceeds $n_{\text{sink}} = 5 \times 10^{13} \text{ cm}^{-3}$. A sink particle is characterized by two important parameters, a mass and a sink radius (R). The region within R around the sink particle is called the “interaction region”, inside which gas particles are accreted onto the sink particle.

As sink particle candidates, we first mark the gas particles with densities greater than n_{sink} . To determine which gas particle should be replaced by a sink particle, we impose the following additional criteria (Hubber et al. 2013).

(i) Overlap criterion:

The interaction region of a newly formed sink particle should not overlap with that of a preexisting sink particle j ,

$$r_{ij} > X_{\text{sink}} h_i + R_j, \quad (1)$$

where h_i is the smoothing length of the candidate gas particle i , X_{sink} is an order of unity parameter which is set to be 4, r_{ij} is the separation between the candidate gas particle i

and the preexisting sink particle j , and R_j is the sink radius of the preexisting sink particle j . Here, $X_{\text{sink}} h_i$ is the sink radius if the gas particle i is replaced by the sink particle.

(ii) Minimum gravitational potential:

The particle should reside at the local gravitational potential minimum. We calculate the gravitational potential around the candidate particles. Then we examine whether they reside at the potential minimum among other gas particles within h_i around the candidate particle. If not, we exclude the gas particle from the candidates.

(iii) Hill criterion:

The candidate gas particle (with index i) should have a sufficiently high density to contract under the disrupting tidal force from preexisting sink particle(s),

$$\rho_i > \rho_{\text{Hill}} \equiv \frac{3X_{\text{Hill}} a_{ij}}{4\pi G r_{ij}}, \quad (2)$$

where G is the gravitational constant, ρ_i is the density of the candidate gas particle i , a_{ij} is the gravitational acceleration caused by the sink particle j , and X_{Hill} is an order of unity parameter which is set to be 4.

The radius of the newly formed sink particle i is set to be $X_{\text{sink}} h_i$, which is $\sim 20 \text{ AU}$ in our calculations.

We assume that a sink particle accretes all the gas particles in the interaction region. Note that the prescription likely overestimates the accretion rate (Bate et al. 1995; Hubber et al. 2013), because no gas particles are allowed to exist around the sink particles. The surrounding gas particles outside the interaction region are also accelerated toward the sink particle by the negative pressure gradient. We allow merging of sink particles, when the separation of two sinks becomes smaller than the sink radius or the stellar radius (R_* , see Section 2.5.1). This is necessary because the giant protostars have radii comparable to the sink radius when they are accreting the matter at a rate of $\sim 0.1\text{--}1 M_\odot \text{ yr}^{-1}$, the typical values in the DC model (e.g. Hosokawa et al. 2013). We conserve the mass and momentum of the sink particles before and after merging. The angular momentum is also conserved, and the original orbital angular momentum is distributed to the gas just outside the interaction region. However, we do not exactly follow such an angular momentum redistribution because the detailed hydrodynamics during the merger is not fully resolved near the sink. Since each protostar experiences the merger event less than once during the simulations, the uncertainty will not significantly change our results.

2.5 Stellar evolution model

We employ an analytic model to estimate the radius, luminosity, and effective temperature of an accreting protostar. Our model reproduces well the evolution of the protostar properties for various accretion histories. The model has been tested with more detailed calculations that solves the stellar interior structure equations (e.g. Hosokawa et al. 2013; Sakurai et al. 2015). In this study, we adopt an even simpler model with the following two evolutionary stages: (1) the supergiant protostar phase, and (2) zero-age main sequence (ZAMS) phase.

2.5.1 Supergiant protostar phase

Hosokawa et al. (2012, 2013) show that, with a high accretion rate exceeding $\dot{M}_{\text{crit}} = 0.04 M_{\odot} \text{ yr}^{-1}$, the evolution of the stellar radius is well approximated by the following relation

$$R_* = 38 \text{ AU} \left(\frac{M_*}{1000 M_{\odot}} \right)^{1/2}, \quad (3)$$

which means that the star has a very large radius and remains bloated as the stellar mass increases, independent of different accretion rates. During this stage, the stellar effective temperature is almost locked at $\simeq 5000 \text{ K}$ owing to very strong temperature dependence of H^- opacity (e.g. Hayashi 1961). The protostar only emits a small amount of ionizing photons with such a low effective temperature. The resulting UV feedback is thus too weak to disturb the accretion flow (e.g. Hosokawa et al. 2016). Even if the accretion rate falls below \dot{M}_{crit} , the protostar remains bloated for about ten times the Kelvin-Helmholtz (KH) timescale (Sakurai et al. 2015),

$$t_{\text{KH, surf}} = 1000 \text{ yr} \left(\frac{M_*}{500 M_{\odot}} \right)^{1/2}. \quad (4)$$

As an input to our analytic model, we estimate the accretion rate onto the protostar by averaging instantaneous rates onto the sink particle over every 30 years. We assume that the protostar is in the supergiant phase described by eq. (3) when the estimated accretion rate is higher than the critical value \dot{M}_{crit} . When being in the supergiant phase, a protostar emits little amount of ionizing photons. The protostar remains in the supergiant phase unless the accretion rates fall below \dot{M}_{crit} for a duration longer than $t_{\text{KH, surf}}$.

2.5.2 Zero-age main sequence phase

When the above conditions for the supergiant phase are not satisfied, the protostar begins to contract owing to the radiative energy loss, leaves the supergiant phase (Sakurai et al. 2015), and enters the so-called KH contraction phase. The stellar effective temperature rapidly rises up to $\sim 10^5 \text{ K}$ during KH phase. After the contraction over a KH timescale, the accreting star turns to follow the mass-radius relation of the ZAMS stars.

For our analytic model, we simply assume that the protostar is on the ZAMS if not in the supergiant phase. We adopt our previous results of the stellar evolution calculations for the ZAMS stars, i.e., the radius, luminosity, and effective temperature are tabulated as functions of the stellar mass. We also assume that the star quickly returns back to the supergiant phase once the accretion rate exceeds \dot{M}_{crit} .

Since we ignore the finite KH timescale for the supergiant star to contract toward the ZAMS star, our above prescription overestimates the stellar emissivity of the ionizing radiation. As we will see in Section 4, however, the ionizing photons hardly affect the accretion flow in our simulations even with our simplified stellar model.

2.6 Transfer of ionizing radiation

We calculate photo-ionization of neutral hydrogen and the resulting heating using a ray tracing scheme proposed by

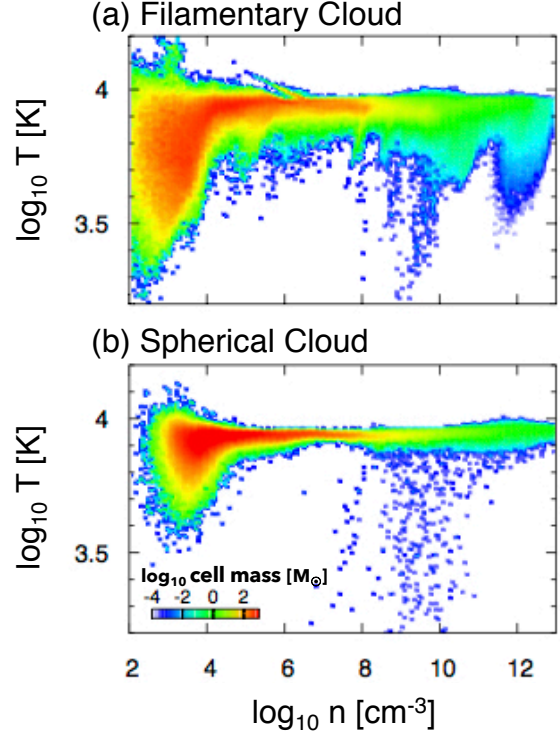


Figure 2. Mass distributions on the density-temperature phase diagram for (a) the filamentary cloud and (b) spherical cloud. The snapshots are taken when the maximum density exceeds 10^{12} cm^{-3} in the early collapse stage. We here divide the whole domain into 200×200 cells. The color map represents the gas mass contained within each cell.

Susa (2006). The optical depth of ionizing radiation, τ_{UV} , from a light source to the particle i is evaluated as the sum of the local optical depth, $\sum_j d\tau_{\text{UV},j}$. Here, $d\tau_{\text{UV},j}$ is the optical depth from the particle j to a particle located at the upstream of particle j . We then calculate the photon number which is locally consumed by the interaction with the neutral hydrogen. Since the optical depth of one SPH particle is often large, we use the so-called photon conserving method (Kessel-Deynet & Burkert 2000; Abel et al. 1999), where the photo-ionization rate k and the photo-heating rate Γ are given by (Rybicki & Lightman 1979):

$$k = -\frac{1}{4\pi r^2} \frac{d}{dr} \int_{13.6 \text{ eV}/h}^{\infty} \frac{L_{\nu} e^{-\tau_{\nu}}}{h\nu} d\nu, \quad (5)$$

$$\Gamma = -\frac{1}{4\pi r^2} \frac{d}{dr} \int_{13.6 \text{ eV}/h}^{\infty} \frac{L_{\nu} e^{-\tau_{\nu}}}{h\nu} (h\nu - 13.6 \text{ eV}) d\nu \quad (6)$$

We discretize the above equations and take volume averages.

3 RESULTS

3.1 Early collapse phase

In Chon et al. (2016), we followed the cloud evolution until the central density reaches 10^8 cm^{-3} . In both runs, the cloud collapses in a “runaway” manner until a protostellar core appears at the center of the cloud. During the collapse, the gas cools by H atomic cooling. Fig. 1 shows the snapshots

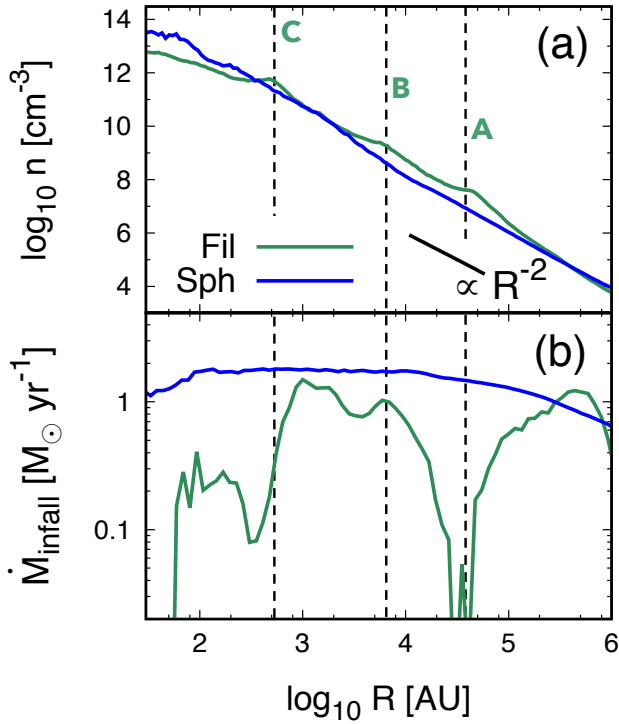


Figure 3. (a) The radial density profiles for the filamentary (green) and the spherical clouds (blue) in their latest stages of the run-away collapse. The vertical dashed lines marked as A, B, and C indicate three characteristic scales where the filamentary cloud shows the density bumps. The power-law profile $n \propto R^{-2}$ is also shown with the short black solid line for the reference. (b) The radial profiles of the mass infall rate (\dot{M}_{infall} , eq 7).

when the central density reaches 10^{12} cm^{-3} . In one case, a filamentary cloud is formed by the strong tidal field from the nearby galaxy (left top panel in Fig. 1) whereas the other cloud contracts nearly spherically (right bottom panel in Fig. 1). We call the former as “filamentary cloud” and the latter as “spherical cloud”.

Fig. 2 shows the density-temperature phase diagram within 10 pc from the cloud center. Both clouds collapse almost isothermally on a high-temperature track between 8000 and 10000 K, while the adiabatic expansion cools some gas particles slightly below 8000 K. In some cases, the adiabatic expansion is followed by H_2 formation as its collisional dissociation rate decreases with decreasing the temperature. Especially at $n \gtrsim 10^8 \text{ cm}^{-3}$, a small number of gas particles cool below 5000 K with the aid of rapid H_2 formation by 3-body reaction. Inayoshi et al. (2014) point out that the above process triggers the chemical and thermal instability in the early collapse phase.

Fig. 3(a) shows the radial density profiles for the filamentary (green) cloud and for the spherical (blue) cloud when the cloud density reaches 10^{13} cm^{-3} . In both the cases, the density profile approximately follows $n \propto R^{-2}$ (black), which is expected for self-similar collapse of an isothermal cloud (Larson 1969). However, in the filamentary cloud, the profile shows small bumps. We mark them in Fig. 3(a) by the dashed lines and label them as A, B, and C from low to

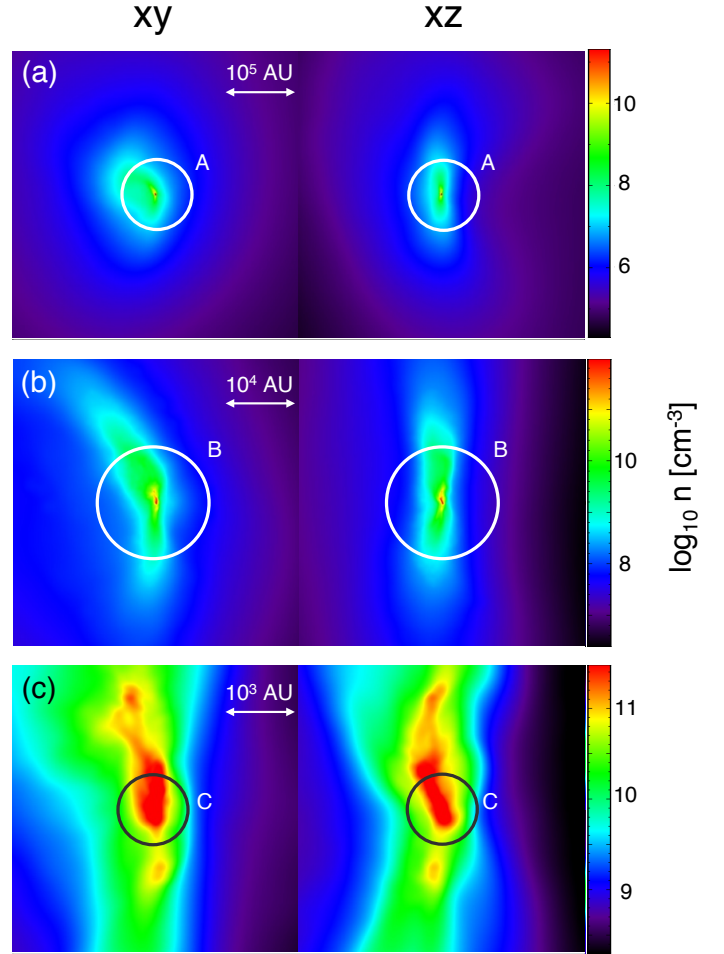


Figure 4. The projected density maps within the filamentary cloud when the maximum density reaches 10^{12} cm^{-3} . The physical scales become smaller from the top to bottom panels. The left and right panels show the maps projected onto different planes, which are perpendicular to each other (labeled as “xy” and “xz” planes). The solid circles (A, B, and C) represent the scales presented in Fig. 3.

high density. Fig. 3(b) shows the radial profiles of the mass infall rate (\dot{M}_{infall}) measured at the distance R ,

$$\dot{M}_{\text{infall}}(R) \equiv 4\pi R^2 \rho v_{\text{rad}}, \quad (7)$$

where ρ is the density and v_{rad} is the radial velocity of gas. We find that the spherical cloud has $\dot{M}_{\text{infall}} \gtrsim 1 M_{\odot} \text{ yr}^{-1}$ at $R \lesssim 10^6 \text{ AU}$. The filamentary cloud also has $\dot{M}_{\text{infall}} \gtrsim 1 M_{\odot} \text{ yr}^{-1}$ at $R \lesssim 10^6 \text{ AU}$. However, around the indicated regions A and C, \dot{M}_{infall} is smaller than $1 M_{\odot} \text{ yr}^{-1}$. As we will see later in Section 3.2.2, the filament starts to fragment at A and C in the later accretion phase.

Fig. 4 shows the projected density distribution around the protostar in the filamentary cloud. The left and right panels show the projections from the different directions and we label them as “xy” (left) and “xz” (right). In the region larger than A, the cloud has round shape projected onto “xy” plane while it is elongated and shows a filamentary structure in the “xz” plane. Near region B, the cloud shows a clear filamentary structure. Around scale C, the filament

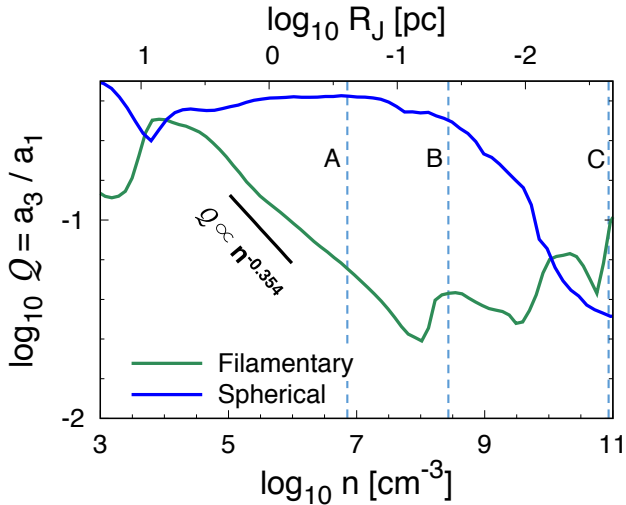


Figure 5. Evolution of the axial ratio Q during the collapse of the filamentary (blue) and spherical clouds (green). The ratio Q is defined as a_3/a_1 , where a_1 and a_3 are the lengths of the longest and shortest axes. The upper horizontal axis represents the corresponding Jeans length (eq. 8) with the temperature fixed at 8000 K. The vertical dashed lines A, B, and C show the reference scales shown in Fig. 3(a).

starts to fragment into multiple clumps. We will see the cloud also fragments at scale A at 6800 yr after the central protostar formation (Section 3.2.2).

To quantify the deviations from spherical collapse, we approximate iso-density volumes around the cloud center by a series of ellipsoids. In Fig. 5, we show how the axial ratio $Q \equiv a_3/a_1$ of the iso-density contour varies with different densities for the filamentary (blue) and the spherical (green) clouds. Here, a_1 and a_3 are the lengths of the axes which have the largest and smallest magnitudes, respectively. The filamentary cloud has smaller axial ratios than the spherical cloud. For example, at $n = 10^8 \text{ cm}^{-3}$, the filamentary and spherical clouds have the axial ratios of ~ 0.03 and ~ 0.3 , respectively. In Fig. 5, we also show the Jeans length (R_J) as a function of the gas density (n) with the fixed temperature $T = 8000 \text{ K}$,

$$R_J = 0.22 \text{ pc} \left(\frac{n}{10^7 \text{ cm}^{-3}} \right)^{-1/2}. \quad (8)$$

The axial ratio decreases at $n \gtrsim 10^{10} \text{ cm}^{-3}$ in the spherical cloud because the disk-like structure appears around owing to the finite angular momentum. Contrastingly, the small axial ratio at $n \gtrsim 10^6 \text{ cm}^{-3}$ of the filamentary cloud is not caused by disk formation. The corresponding Jeans scale at this density is much larger than the scale where the angular momentum support is strong at this epoch. Rather, the small axial ratio is explained by development of a bar in isothermal gas. Hanawa & Matsumoto (2000) suggest a relation $Q \propto n^{-0.354}$ in linear regime. We see that Q actually follows this relation in the filamentary cloud (black solid line). At $n \sim 10^8 \text{ cm}^{-3}$, Q reaches 0.03 and enters the nonlinear regime (Tsuribe & Omukai 2006; Chiaki et al. 2016).

Note that the elongation, i.e., the decrease of Q , is not

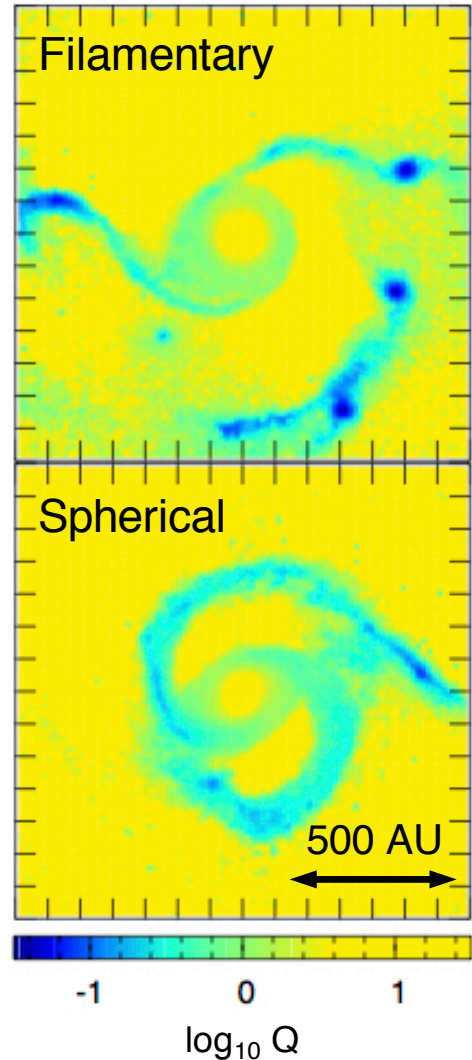


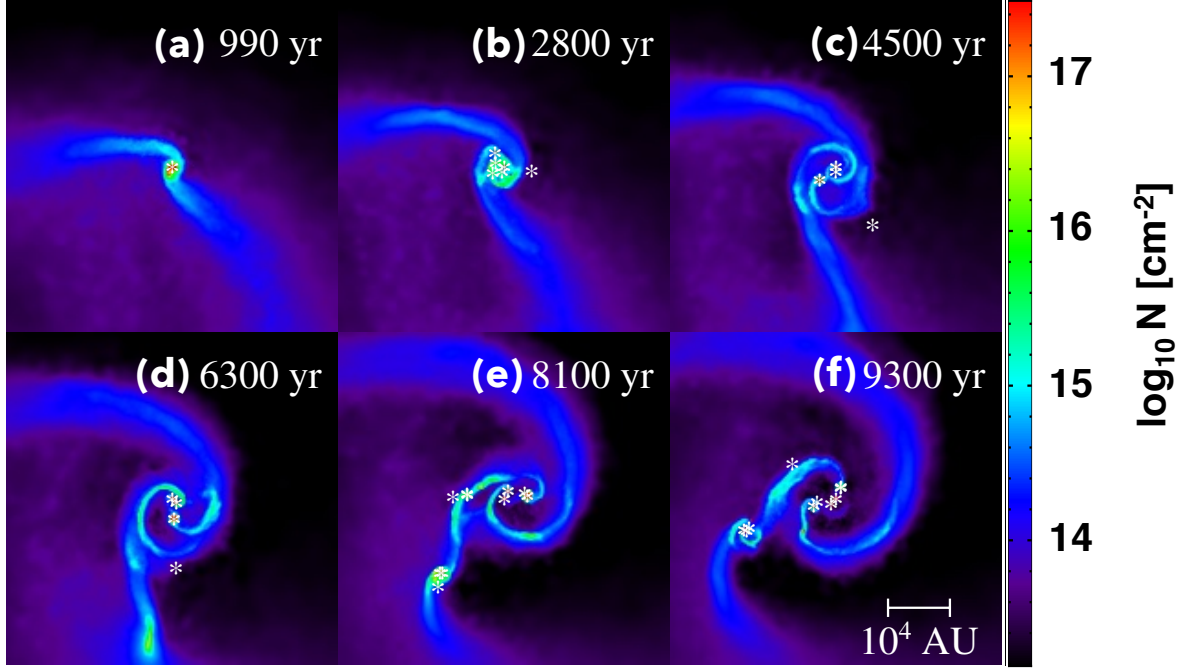
Figure 6. Distributions of Toomre Q parameter (eq. 9) around the central protostar for the filamentary (top) and the spherical (bottom) clouds. The snapshots are taken at $\simeq 1500 \text{ yr}$ after the central protostar is formed.

entirely driven by the tidal torque from the nearby massive galaxy. The tidal radius is about 1 pc and thus has almost no effect at smaller length scales. The initial perturbations are seeded by the tidal torque, and grow through isothermal collapse in the filamentary cloud.

3.2 Later accretion phase

After the central protostar is formed, the infalling gas with finite angular momentum is accumulated to form a circumstellar disk. In the self-gravitating gas disk, angular momentum is transferred outward by the gravitational torque and the central protostar is able to accrete and grow in mass. When the disk becomes massive enough, however, it bears multiple fragments. In this section, we study the evolution of the protostars and the circumstellar disks.

I. Filamentary Cloud



II. Spherical Cloud

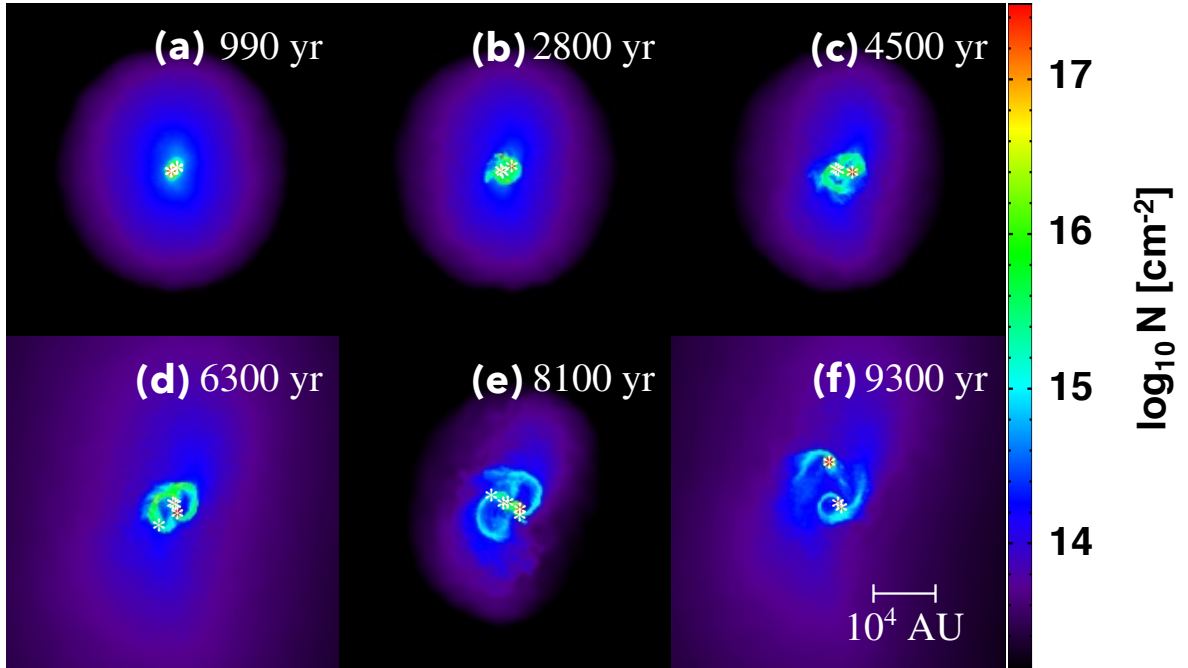


Figure 7. Face on view of the evolving disk and stellar systems in the filamentary (top) and spherical (bottom) clouds. The white asterisks and colormaps represent the protostars and column density of the surrounding gas. The time is measured from the epoch when a protostar first appears in the clouds.

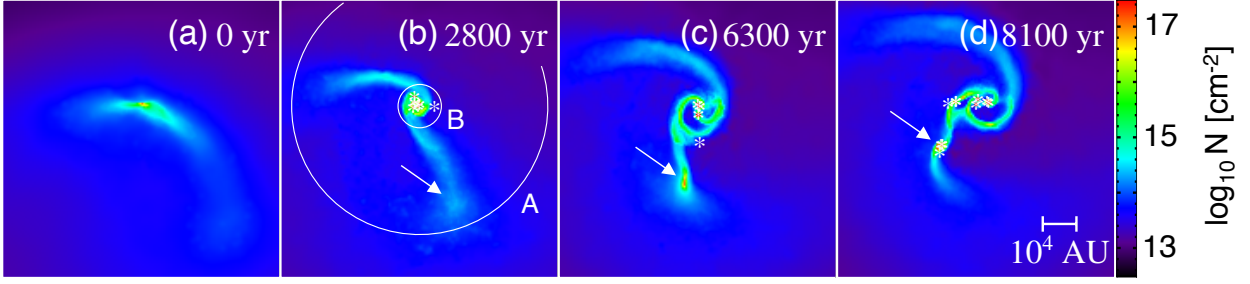


Figure 8. Filament fragmentation occurring in the filamentary cloud. The arrows indicate where a star-disk system forms through such an event. In panel (b), the white circles indicate the different spatial scales A and B appeared in Fig. 3.

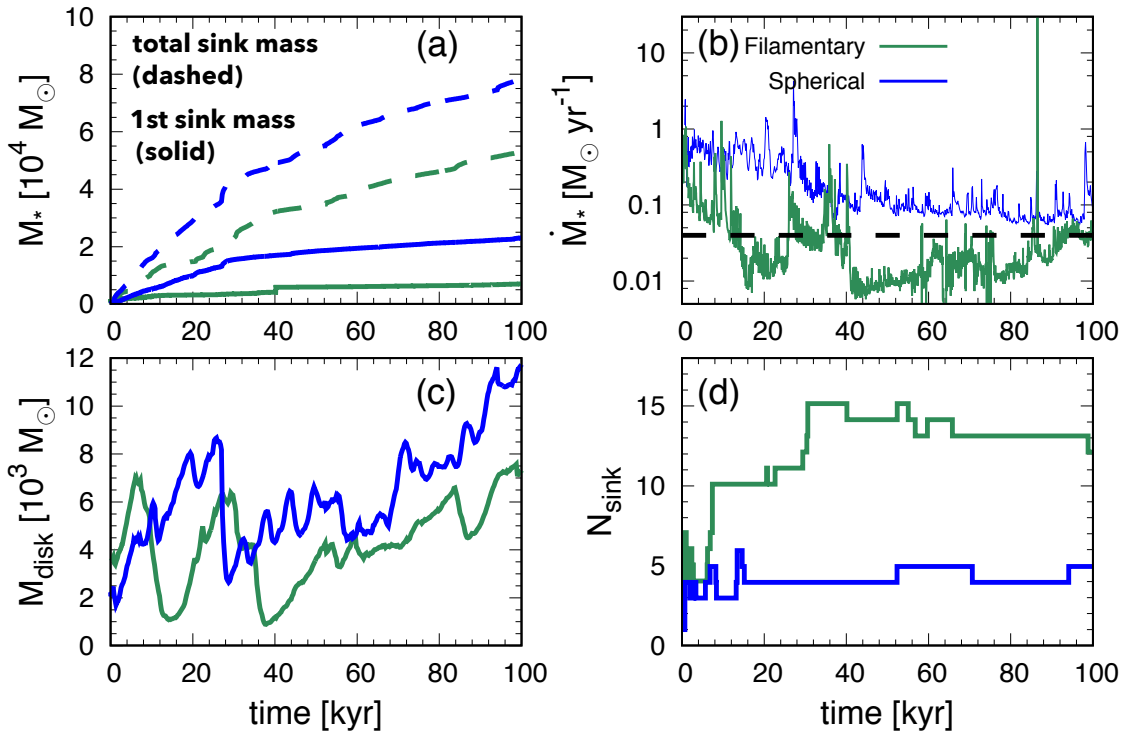


Figure 9. Evolutions of (a) the stellar mass, (b) accretion rate, (c) disk mass, and (d) number of the protostars for the filamentary (green) and spherical (blue) clouds. In panel (a), the solid and dashed lines represent the masses of the primary protostars and total stellar masses. The primary protostar is the one which is first formed in the calculation. In panel (b), the horizontal dashed line shows the critical accretion rate, below which the star contracts to the ZAMS phase (see Section 2.5). The accretion rate is averaged over 30 yr.

3.2.1 The evolution of the star-disk system

A heavy circumstellar disk quickly undergoes gravitational fragmentation. To quantify the gravitational instability, we calculate the Toomre- Q parameter defined by

$$Q = \frac{c_s \Omega}{\pi G \Sigma}, \quad (9)$$

where c_s is the sound speed, Ω is the orbital frequency, and Σ is the surface density of the disk. Fig. 6 shows the distribution of Q parameter on the disk plane at 1500 yr after the protostar is formed. Inside the disk, Q is order of unity while it is smaller than unity along the spiral arms (Gammie 2001; Takahashi et al. 2016). These arms quickly fragment into multiple clumps, where the Q is smaller than unity ($Q \sim 0.1$).

The most unstable length- and mass-scales for the gravitational fragmentation are given by $\lambda \sim c_s / \Omega$ and $M_{\text{frag}} \sim \pi (\lambda/2)^2 \Sigma$ where $Q = 1$ has been assumed. With the typical temperature and surface density in our simulations, these scales are

$$\lambda = \frac{\pi c_s^2}{G \Sigma} = 17 \text{ AU} \left(\frac{T}{8000 \text{ K}} \right) \left(\frac{10^5 \text{ g cm}^{-2}}{\Sigma} \right), \quad (10)$$

$$M_{\text{frag}} = \frac{\pi^3 c_s^4}{4 G^2 \Sigma} = 2.5 M_\odot \left(\frac{T}{8000 \text{ K}} \right)^2 \left(\frac{10^5 \text{ g cm}^{-2}}{\Sigma} \right)^2. \quad (11)$$

We find that the initial fragment mass is $\sim 5 M_\odot$, in good agreement with the above simple estimation.

Fig. 7 shows the development of multiple protostar-disk systems for the filamentary and spherical cases, where the

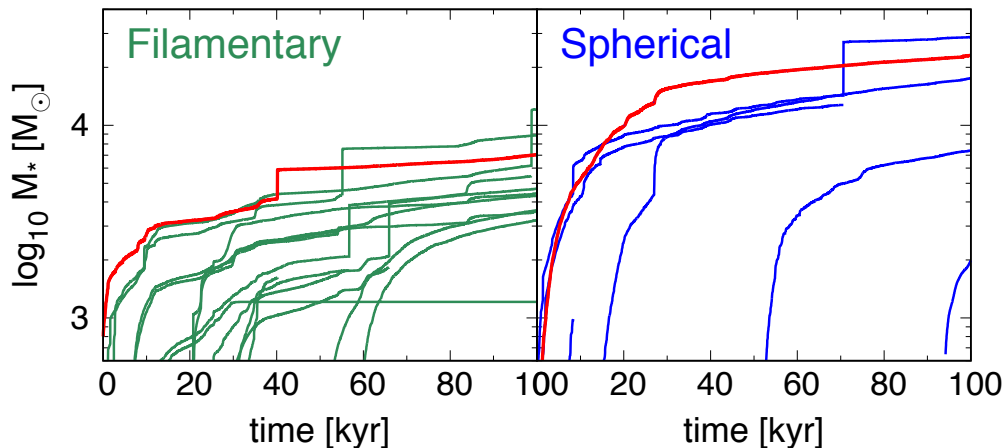


Figure 10. Mass evolution of all the protostars in the filamentary (left) and the spherical (right) clouds. The stellar merger events are marked with the vertical jumps seen in some lines. Note that another line ends at the same point, representing the merger partner. The red line shows the mass evolution of the primary protostar.

color scales indicate the column density distribution projected onto the disk plane. The circumstellar disk continuously acquires mass and grows in mass and size (Fig. 7-Ia and IIa). Then spiral arms are excited, which further fragment into multiple clumps that finally contract to become protostars (Fig. 7-Ib and IIb). At early epochs, some of the newly formed protostars rapidly fall onto the central protostar. The inward migration is promoted by the interaction with the gas inside the disk (the so-called Type-I migration).

The gas density near the disk center decreases with time because remaining protostars accrete the surrounding gas (Fig. 7-Ic and IIc). This makes the gas-star interaction less efficient and the migration toward the central protostar ceases. More than three protostars are formed inside the disk and they remain on stable orbits for several tens of the disk rotation period. These features are common in both the filamentary and the spherical clouds.

In the spherical cloud, only a single circumstellar disk is formed around the cloud center. The multiple stellar system formed via fragmentation of the primary disk is stable, and no stars are found to be ejected from the disk until the end of our calculation ($t \sim 0.1$ Myr). The separations between the protostars are smaller than the disk size of $\lesssim 10^4$ AU at 0.1 Myr.

In the filamentary cloud, another star-disk system is formed at $\sim 10^4$ AU from the cloud center as seen in Fig. 7-Ie. In panel (b), we indicate the radii corresponding to A and B in Fig. 3 by white circles. The filament starts to fragment just near the circle A, where the filament’s axial ratio is small enough and an overdense clump can grow in a non-linear fashion (see Section 3.1). The clump soon migrates toward the cloud center (panel d). Since angular momentum is difficult to be extracted during its migration due to the low gas density, the final separation between the two star-disk systems is set by the angular momentum barrier. The separation is larger than that found in the spherical cloud. The filamentary collapse tends to generate multiple star-disk systems that are well-separated.

3.2.2 Stellar mass growth

Fig. 9(a) shows the evolution of the total protostellar mass (dashed) and the mass of the primary protostar (solid line). Fig. 9(b) shows the evolution of the mass accretion rate onto the primary protostar. Fig. 10 shows the mass evolution of all the protostars found in each simulation. In these figures, the green and blue lines represent the results for the filamentary and spherical clouds, respectively.

The accretion rates are highly variable with time. Such rapid variations have been often seen for the mass accretion through a self-gravitating circumstellar disk, and is known as “episodic accretion” (e.g. Vorobyov et al. 2013). We notice that the accretion rate suddenly increases up to ~ 1 – $10 M_\odot \text{ yr}^{-1}$ at $t \sim 27$ kyr in the filamentary cloud. At this epoch, the primary protostar experiences the three body interaction with other protostars. The close encounter of the primary protostar with another one excites strong density enhancement and causes a large amount of the gas to fall onto the primary protostar.

In the spherical cloud, stars grow in mass with a rate of $0.1 - 1 M_\odot \text{ yr}^{-1}$ until the end of the calculation. The rates are much higher than the critical accretion rate, $\dot{M}_{\text{crit}} = 0.04 M_\odot \text{ yr}^{-1}$, and thus the stellar envelope remains expanded to the radius of several $\times 10$ – 100 AU. In the spherical gas cloud, the ionizing photon emissivity is smaller than the number of hydrogen atoms infalling toward the center per unit time (Sakurai et al. 2015), and hence the protostars cannot fully ionize the surrounding gas.

In the filamentary cloud, however, \dot{M}_* decreases occasionally below \dot{M}_{crit} . Fig. 9(c) shows the evolution of the disk mass, where the disk mass is defined as the gas mass with $n > 10^9 \text{ cm}^{-3}$. At $t \sim 10$ kyr, another protostar is formed in the disk, and both \dot{M}_* and the disk mass rapidly decrease because the newly born protostar accretes the gas in its surrounding. The primary protostar can then contract toward the ZAMS under the slow accretion, and the emissivity of ionizing photons increases. Nevertheless, the ionizing radiation does not prevent the mass accretion because the surrounding gas, even if it is ionized, is strongly bound by

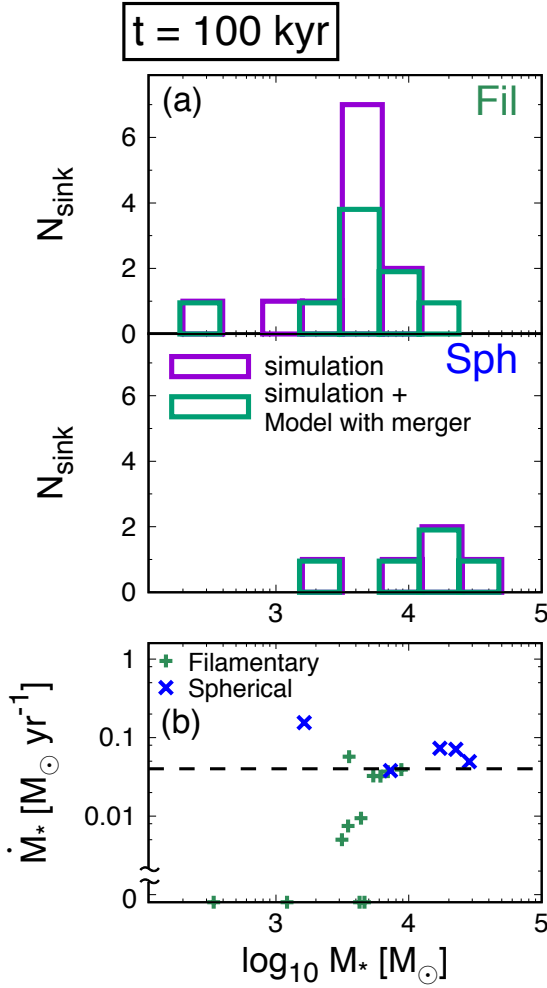


Figure 11. (a) Stellar mass distributions at $t = 100$ kyr for the filamentary (top) and spherical (bottom) clouds. In each panel, the purple histograms show the simulation results, and the green ones show the modified distributions with “Model with merger”. In this model, we first pick up protostar pairs which experience close encounters with < 200 AU and assume these pairs have merged into single protostars. The mass of a combined protostar is the total mass of the original pair. (b) Mass accretion rates (\dot{M}) against the stellar masses (M_*) at $t = 100$ kyr for the filamentary (green) and the spherical (blue) clouds. The dashed line represents the critical mass accretion rate, below which the protostar contracts into the ZAMS phase.

the protostar. By $t \sim 25$ kyr, the gas is quickly accumulated around the protostar and the accretion rate rises over the critical value. The star recovers the supergiant phase again. We will discuss the efficiency of the ionizing radiation feedback later in Section 4.

Fig. 9(d) shows the number of the protostars found in the simulation. The disks around the protostars become more stable with time in both clouds. In fact, the total stellar mass grows at a faster rate than the disk mass. Thus, the Toomre- Q becomes larger with increasing time (see eq. 9). The number of protostars hardly changes after $t \sim 40$ and 20 kyr for the filamentary and the spherical clouds, respectively. In the filamentary cloud, fragmentation still continues at later time than in the spherical cloud. This is because the

$(t = 100 \text{ kyr})$	total	survived	ejected	binary
Filamentary	25	13	3	7
Spherical	13	5	0	4

Table 1. Statistical properties of protostars at $t = 100$ kyr. Each column show the number of protostars in total, survived, ejected, and belong to any binaries at $t = 100$ kyr from left to right.

fragmentation also occurs at the filament far from the disk (see Figs. 7-Id, Ie, and 8). The filament fragmentation itself is not stabilized by the growth of the protostars. For example, filament fragmentations take place at $t \sim 8$ and 30 kyr. We can see that the number of protostars suddenly increases around these epochs.

3.2.3 Mass distribution of the protostars

Fig. 11(a) shows the mass distributions of the protostars at $t = 100$ kyr for the filamentary (top) and the spherical (bottom) clouds. The purple histograms show the mass distribution obtained in the simulations. Since the resolution of our simulation is limited, further migration within ~ 100 AU cannot be followed accurately (Section 5.4). Since the stellar radius is also of the order of ~ 100 AU, the two protostars are likely to merge, and the stellar mass of each star obtained in our simulation is probably underestimated. Once a protostar pair gets closer than 200 AU, they are assumed to merge. Thereafter we treat the pair as a single protostar, and just sum the masses of the merging protostar pair. We refer this model as “Model with merger” (green histograms in Fig. 11).

For the filamentary cloud, the stellar mass distribution is concentrated at $3000\text{--}6000 M_\odot$. Fig. 11(b) summarizes how rapid mass accretion still continues depending at the epoch of $t = 100$ kyr. The dashed line represents the critical mass accretion rate below which the supergiant star contracts into the main sequence phase. In the spherical cloud, protostars grow at rates $\gtrsim 0.1 M_\odot \text{ yr}^{-1}$. Even the most massive one remains in the supergiant phase. Consequently, the protostars cause only weak ionizing radiation feedback for entire period of our calculation. In the filamentary cloud, the accretion rate decreases with time and becomes smaller than the critical value for most of the protostars at $t = 100$ kyr. The total ionizing photon emissivity increases to cause strong radiation feedback. However, as we will see in Section 4, the ionizing radiation does not completely prevent mass accretion in our calculation, because the accreting gas is strongly bound by the central stars.

3.2.4 Merger and ejection of protostars

In our simulations, protostars interact gravitationally with other protostars. The close encounter of protostars results in various events such as binary formation, merger, and ejection of the protostars. Mergers mainly take place within $\lesssim 1\text{--}2$ kyr after the disk fragmentation because the surface

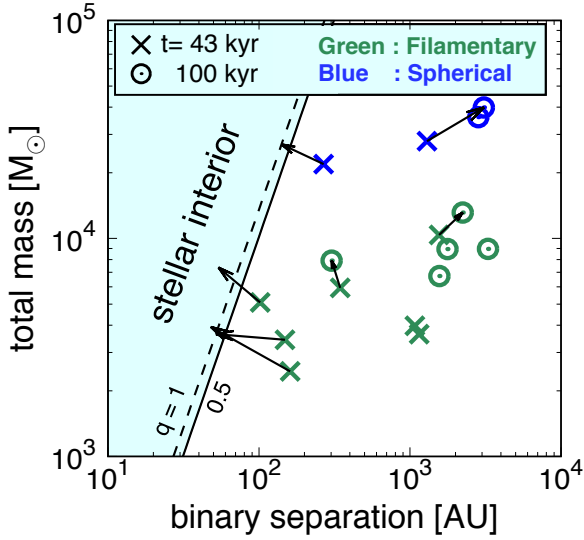


Figure 12. Appearance and evolution of the stellar binaries in the filamentary (green) and spherical (blue) clouds. The different symbols represent the different epochs $t = 43$ kyr (crosses) and 100 kyr (circles). The solid and dashed lines show the radii of the binary stars, assuming they are in the supergiant phase (eq. 3) with the different mass ratios of $q = 0.5$ and 1 . Once a binary enters the shaded region, it is assumed to be merged in our simulations. The arrows indicate the evolution of the same binaries between the two presented epochs.

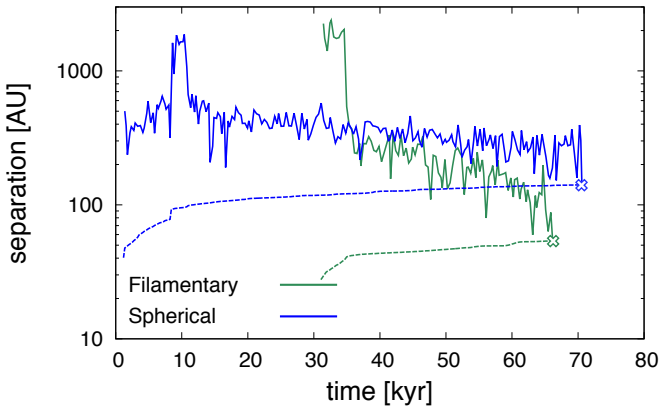


Figure 13. Examples of the time evolution of the binary separation. Shown are merged binaries typical in the filamentary (green) and spherical (blue) clouds. The solid and dashed lines represent the binary separation and the radii of the binary stars. The start and end points of each line correspond to the epochs of the binary formation and merger.

density of the disk decreases and the disk-star interaction becomes inefficient after the sequence of fragmentation. Table 1 summarizes the number of protostars which are formed in the simulation. We also list the number of survived, ejected, and belong to any binaries at $t = 100$ kyr for the filamentary and the spherical clouds. A protostar is assumed to be ejected once the velocity exceeds the escape velocity (v_{esc})

of the cloud,

$$v_{\text{esc}} = \sqrt{\frac{2GM_{\text{enc}}(< R)}{R}}, \quad (12)$$

where R is the distance from the center of mass. Once a protostar pair becomes gravitationally bound, the pair is classified as a binary. We judge a pair is bound if the total energy (E_{tot})

$$E_{\text{tot}} = \frac{m_1 v_1^2}{2} + \frac{m_2 v_2^2}{2} - \frac{Gm_1 m_2}{r} \quad (13)$$

is negative, where m_i is the mass of the protostar member, v_i is the relative velocity to the center of mass, and r is the separation of the members ($i = 1, 2$).

Fig. 12 shows the distributions of separations against the total mass of binaries at different epochs of $t = 43$ (cross) and 100 kyr (open circle). We present the evolution of the mass and the separation of the binaries by arrows. The solid and dashed lines represent the stellar radius under the mass ratios (q) with 1 and 0.5 , respectively. Inside the shaded region, the separation is smaller than the stellar radius. We confirm the binaries usually have $q \gtrsim 0.5$. We also assume both of the member stars are accreting material at a rate of $> 0.04 M_{\odot} \text{ yr}^{-1}$ and stars are in the supergiant phase (eq. 3). At $t = 43$ kyr, some binaries have separations slightly larger than the stellar radius. These stars grow in mass and radius with time (eq. 3) and finally coalesce. At $t = 100$ kyr, the survived binaries have typical separations of a few times $\sim 10^3$ AU, which is an order of magnitude larger than the stellar radius. These binaries are so stable that they will finally evolve into BH binaries after the stellar lifetime. We will discuss the evolution of these binaries in Section 5.2.

Fig. 13 shows the evolution of the separation of the merged binaries. Here, we show examples both of the filamentary (green) and of the spherical (blue) clouds. The solid and dashed lines show the evolutions of binary separation and the stellar radius, respectively. We combine binary members when their separations become smaller than the stellar radius of more massive star. The separation decreases suddenly from ~ 1000 to ~ 100 AU due to the three body interaction with another protostar (i.e. at 35 kyr in the filamentary cloud). The stellar radius grows gradually with time and the binaries finally merge. Other binary mergers take place in a similar manner.

The survival rate of the protostar in the filamentary cloud is larger than in the spherical cloud. This is due to the filament collapse, in which the typical separations between protostars are larger than those in the disk fragmentation. Furthermore, once a filament fragmentation takes place, the disk mass quickly decreases and the binary separation becomes difficult to shrink ($t \sim 10$ kyr in Fig. 7c). Here, we compare our survival rate of protostars with other studies. The formation and evolution of multiple stellar system in the normal Pop III star formation has been followed by some authors (e.g. Stacy et al. 2016; Greif et al. 2012). They find that about one third of protostars survive at the end of the calculation. In our calculation, the survival rates at $t = 100$ kyr are 52 and 38% in the filamentary and the spherical clouds, respectively. The survival rate in the spherical cloud is similar to their results while that in the filamentary cloud is much larger than the results of the previous studies. We stress that their calculated clouds and our spherical

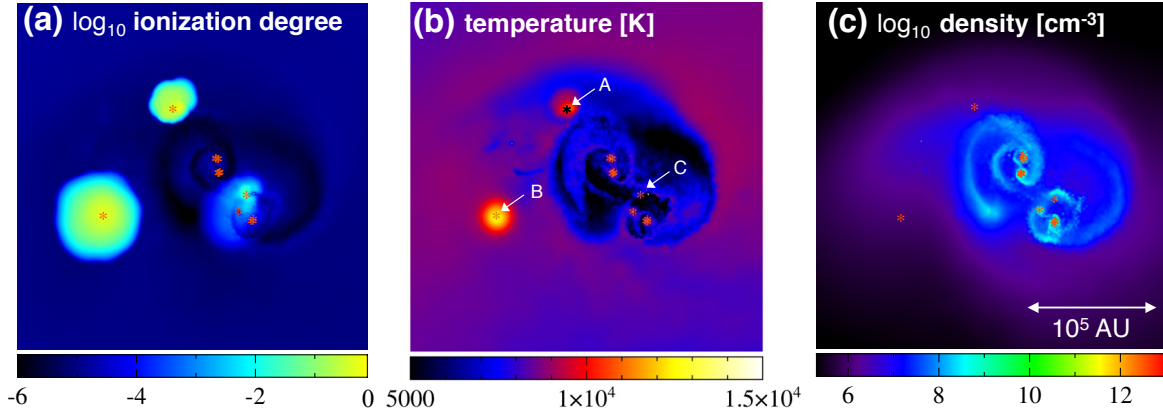


Figure 14. Spatial distributions of (a) hydrogen ionization degree, (b) temperature, and (c) density in the filamentary cloud at $t = 38$ kyr. The asterisks mark the positions of the protostars. In panel (b), protostars which emit a copious amount of ionizing photons are marked with the white arrows and labeled as A, B, and C.

cloud show no filamentary collapse. This fact implies that the survival rate of the protostars is largely determined by the morphology of the collapsing cloud. In this study, the cloud morphology is determined by the tidal field originating from the nearby massive galaxy.

In the filamentary cloud, three ejection events are observed. The ejection is caused by the three body interaction. Meanwhile in the spherical cloud, no protostars are ejected. One reason is that the number of protostars are so small that the chance of three body encounter is much smaller than in the filamentary cloud. The other reason is that the gas rich environment in the spherical cloud suppresses the ejection of protostars (Fig. 9b). We find that when the three body encounter takes place in the spherical cloud, a large amount of gas in the disk is ejected instead of the protostars. In fact, the total gravitational energy released by the binary formation is comparable in both clouds. This energy is transferred to the kinetic energy of the surrounding gas in the spherical cloud.

4 RADIATIVE FEEDBACK EFFECTS

We calculate the radiative feedback from the accreting protostars by adopting the simplified stellar evolution model (Section 2.5). Fig. 14 shows (a) ionization degree, (b) temperature, and (c) density distributions in the filamentary cloud at $t = 38$ kyr. Here, the ionization degree is defined as $y_{\text{HII}}/(y_{\text{HI}} + y_{\text{HII}})$, where y_i represents the abundance of the chemical species i . Three protostars are emitting ionizing photons at this snapshot and we label them as protostars A, B, and C. Protostars A and B are ejected from the central disk by three-body interaction and they create compact H II regions around them whose size is ~ 0.1 pc. Protostar C remains around the center of the disk. We can see ionization degree reaches 0.01–0.1 around protostar C. The temperature around UV emitting protostars only rises by a factor of $\lesssim 2$ than the surrounding neutral gas, since the surrounding gas has already a high temperature (Fig. 14b). Thus, the ionizing radiation causes only minor effects on the protostar evolution in our calculations.

In this section, we investigate the effect of the radia-

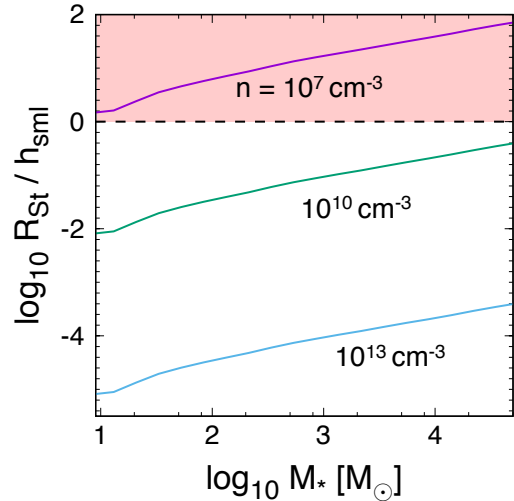


Figure 15. The ratio of the Strömgen radius R_{St} to the smoothing length of the gas particles h_{sml} as functions of the stellar mass. The different lines represent the different densities of $n = 10^7$ (purple), 10^{10} (green), and 10^{13} cm^{-3} (cyan). The horizontal dashed line corresponds to a boundary of $R_{\text{St}} = h_{\text{sml}}$, above which the Strömgen radius is spatially resolved with more than one smoothing length. When calculating h_{sml} with eq. (15), different particle masses are used depending on the density, $1.6 M_{\odot}$ for $n = 10^7 \text{ cm}^{-3}$, and $9.6 \times 10^{-3} M_{\odot}$ for $n = 10^{10}$ and 10^{13} cm^{-3} , the same values as used in the simulations (Section 2.3).

tion feedback in detail and discuss whether the radiation feedback prevents the further mass accretion or not.

4.1 Limitation of the radiative transfer model

One can argue that the radiation feedback is inefficient because, in a high density region, we cannot resolve the initial Strömgen radius (R_{St}), within which ionization and recombination balance. The expansion of the ionized region is mainly driven by the thermal pressure. In order to follow the expansion of the ionized region, we need to first resolve the structure within R_{St} .

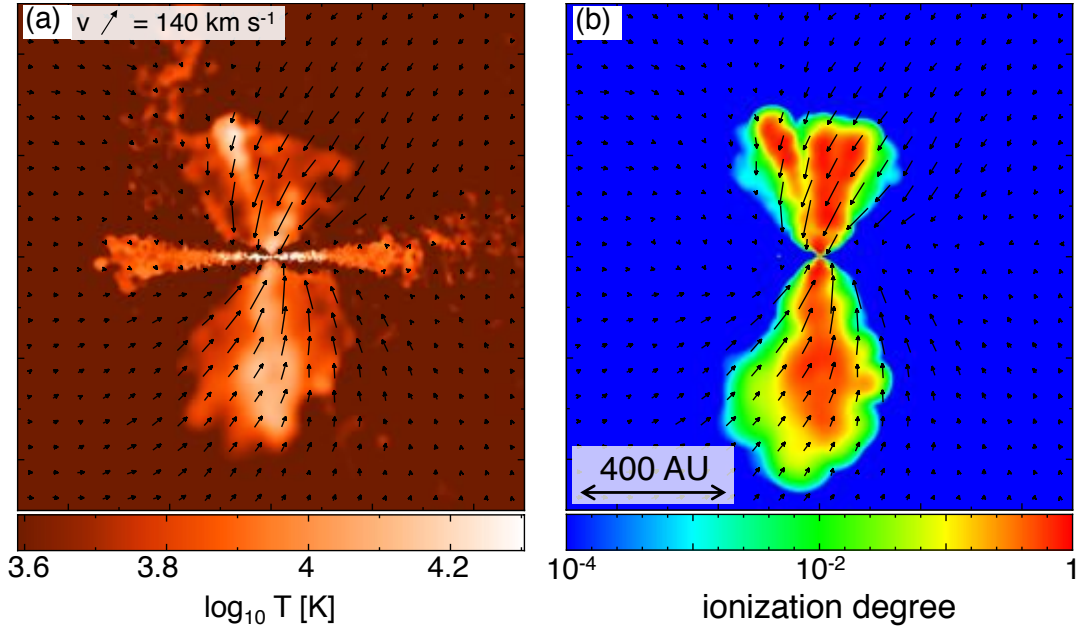


Figure 16. Spatial distributions of the temperature (left) and hydrogen ionization degree (right) around the protostar at 100 years after the particle splitting is performed (see the text). The panels show the edge-on views respect to the circumstellar disk. In each panel, the arrows represent the velocities of the infalling gas.

If the density (\bar{n}) is uniform around the ionizing source, R_{St} can be written as,

$$R_{\text{St}} = \left(\frac{3L_{\text{UV}}}{4\pi\bar{n}^2\alpha_{\text{B}}E_{\text{UV}}} \right)^{1/3} = 300 \text{ AU} \left(\frac{S_{\text{UV}}}{10^{53} \text{ s}^{-1}} \right)^{1/3} \left(\frac{\bar{n}}{10^9 \text{ cm}^{-3}} \right)^{-2/3}, \quad (14)$$

where α_{B} is the case-B recombination coefficient, L_{UV} is the ionizing luminosity, E_{UV} is the mean energy of the ionizing photons, and S_{UV} is the number of the emitted ionizing photons per unit time. To resolve the initial R_{St} , the smoothing length of the SPH particles (h_{sml}) should be sufficiently smaller than R_{St} . The smoothing length h_{sml} are determined in the simulation as

$$N_{\text{neib}}m_{\text{sph}} = \frac{4\pi h_{\text{sml}}^3}{3}\mu m_{\text{p}}n, \quad (15)$$

where $N_{\text{neib}} = 64$ is the number of the neighbor SPH particles to determine h_{sml} , m_{sph} is the particle mass, μ is the mean molecular weight, and n is the density of the gas particle. Equation (15) shows that h_{sml} decreases as we reduce m_{sph} . However, since our goal is to follow the long-term evolution, we cannot reduce the particle mass further.

Fig. 15 shows the ratios of R_{St} to h_{sml} for different stellar masses and ambient densities. Here, S_{UV} is given by the result of Hosokawa et al. (2013) considering the star is contracted to ZAMS. In the dense region $n \gtrsim 10^{10} \text{ cm}^{-3}$, R_{St} is smaller than h_{sml} for the mass range considered. Only in the region with $n \lesssim 10^7\text{--}10^8 \text{ cm}^{-3}$, R_{St} is marginally resolved. In Fig. 14(c), the ejected protostars A and B lie at the density smaller than 10^8 cm^{-3} . This is why the ionized region expands around those protostars. However, protostar C is located inside the disk where $n \gtrsim 10^9 \text{ cm}^{-3}$. With the stellar mass $\sim 10^3 M_{\odot}$, R_{St} is smaller than h_{sml} of the sur-

rounding gas for this case (Fig. 15). Thus, the ionized region is difficult to expand around this protostar.

4.2 Radiation transfer with higher resolution

To further investigate the ionizing radiation feedback, we follow the expansion of the ionized regions accurately by adopting a higher spatial resolution. We focus on the radiation from the most massive protostar in the filamentary cloud. We increase the spatial (and mass) resolution in the polar region, by splitting each gas particle into 10^3 particles. By this procedure, the polar region is filled with a sufficiently large number of gas particles, and it is possible to resolve R_{St} by more than ten times the local smoothing length h_{sml} . We follow the expansion of H II regions for a few hundred years.

Fig. 16 shows the temperature (left) and X_{ion} (right) distributions around the protostar. The arrows indicate the velocity field of the surrounding gas. The ionized region expands in the polar directions. The gas in the polar region is heated up to $2 \times 10^4 \text{ K}$, but the ionized gas continues falling onto the disk, and the expansion of the H II region is soon halted. This is because the temperature of this ionized gas is only by a factor of two to three larger than the neutral gas, and thus is still gravitationally bound by the central star. We evaluate the gravitational radius (R_{B}) at which the gas is bound by the central star as

$$R_{\text{B}} = \frac{GM_{\star}}{c_{\text{s,HII}}^2} = 3.25 \times 10^3 \text{ AU} \left(\frac{M}{10^3 M_{\odot}} \right) \left(\frac{T}{2 \times 10^4 \text{ K}} \right)^{-1} \left(\frac{\mu}{0.6} \right).$$

The protostar mass at this time is about $6000 M_{\odot}$, and R_{B}

is much larger than the size of the ionized region, ~ 400 AU. Thus essentially all the ionized gas is gravitationally bound.

We calculate the mass accretion with and without the ionizing radiation for a few hundred years after the particle splitting. The accretion rates onto the central star show almost no difference between these two runs. The gas within the disk is strongly bound by the central star and not photo-evaporated. We confirm that the infall velocity profiles within the polar region with and without the ionizing radiation remain nearly unchanged and the heating by ionization has little impact on the infalling gas.

Our analytic estimate also shows that the ionized gas will be gravitationally bound until the mass of the central star exceeds $\sim 10^5 M_\odot$. Specifically, we construct the density profile toward the polar region and discuss whether the edge of the ionized region is bound by the central star. More detailed description is given in the Appendix A. Our analysis there supports the simulation result; the ionizing radiation has negligible impact on the accreting matter.

5 DISCUSSION

5.1 Final Mass and Fate of the SMS

Although we have followed the protostellar evolution for ~ 0.1 Myr, it is still way before an SMS collapses into a BH. In order to determine how massive seed BHs are finally left, we need to follow the further evolution for the stellar lifetime ~ 2 Myr. However, it is computationally too expensive to accomplish it. We here estimate the final stellar and BH masses from the final snapshots in our simulations.

Fig. 17 shows the radial profiles of (a) the enclosed gas mass and (b) the gas velocity at the final epoch of our simulations for the filamentary (green) and the spherical (blue) clouds. We see that the gas is outflowing at $R > 7-8$ pc in both clouds, which is caused by tidal disruption by the nearby massive galaxy. The infalling gas within $R < 7-8$ pc can reach the central star within the stellar lifetime, ~ 2 Myr. Panel (a) shows the infalling gas mass is $\lesssim 3 \times 10^5 M_\odot$ for both clouds.

Assuming that no more protostars appear via the fragmentation, and that the existing protostars equally accrete the infalling gas, we can estimate the typical final masses to be $\sim 10^4 M_\odot$ for the filamentary cloud and $\sim 10^5 M_\odot$ for the spherical cloud. These stars are massive enough to collapse into BHs after exhaustion of nuclear fuel (e.g. Umeda et al. 2016; Woods et al. 2017). During the final gravitational collapse, most of the stellar mass is swallowed by the BH (e.g. Shibata et al. 2016; Uchida et al. 2017). Therefore, we expect that the filament cloud yields about ten BHs with $\sim 10^4 M_\odot$ and the spherical cloud produces several BHs with $\sim 10^5 M_\odot$. In what follows we call these BHs as “DCBHs”.

5.2 Evolution of the DCBH binaries

We find that the stellar binaries are formed in the cloud core. Some of them survive until the end of the simulation, without merging with the companion. After their stellar lifetime, they will evolve into massive BH binaries with masses of $10^3-10^5 M_\odot$ and with separations of $10^2 \sim 10^3$ AU (see Fig. 12). One process for the binaries to lose their angular

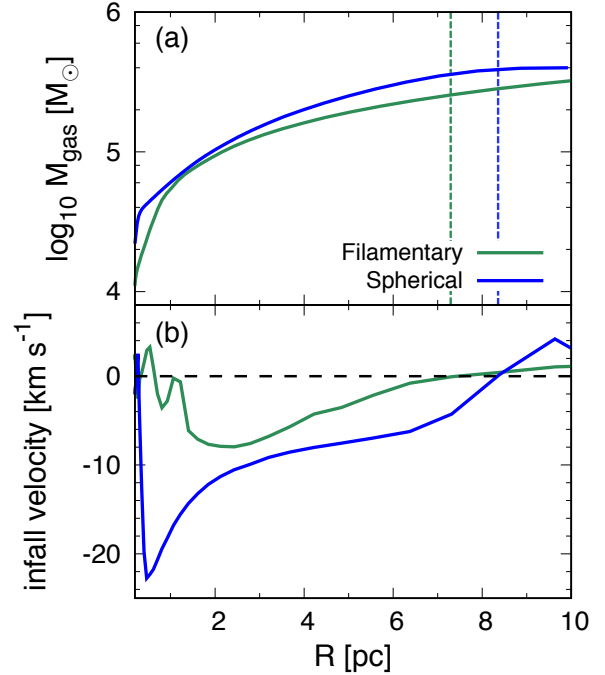


Figure 17. Radial profiles of (a) enclosed gas mass and (b) infall velocity at 0.1 Myr after the birth of the primary protostar for the filamentary (green) and spherical (blue) clouds. The horizontal axis represents the distance (R) from the most massive protostar. In panel (a), the green and blue vertical dashed lines mark the outer boundaries of the clouds, beyond which the gas is moving outward. In panel (b), the horizontal dashed line shows the boundary between the inflow and outflow. Note that a positive value represents the outflow in this plot.

momenta and to coalesce is emission of gravitational waves. The coalescence time is given by (Peters 1964);

$$t_{\text{GW,merge}} = 1.25 \times 10^{11} \text{ yr} \left(\frac{a}{100 \text{ AU}} \right)^4 \left(\frac{M_{\text{BH}}}{10^5 M_\odot} \right)^{-3}, \quad (16)$$

which is about an order of magnitude larger than the Hubble time. Some additional processes to remove the angular momentum, e.g., interactions with surrounding gas or stellar components, are thus necessary for a BH-BH merger to occur.

If the gas or stars are accreted onto a BH, a fraction of the accreted material is scattered and carries away the angular momentum from the system. Kashiwaga & Inayoshi (2016) estimated the number of stars falling onto the central BH, assuming possible star cluster formation. In our simulations, clusters with several to ten stars are formed. Following Kashiwaga & Inayoshi (2016), the relaxation time of these cluster (t_{relax}) is,

$$t_{\text{relax}} \sim 1.6 \times 10^5 \text{ yr} \frac{M_{\text{BH}}}{10^5 M_\odot} \frac{10^3 M_\odot}{\langle M_* \rangle} \left(\frac{r}{\text{pc}} \right)^{-3/2}, \quad (17)$$

where M_{BH} is the central BH mass, $\langle M_* \rangle$ is the average mass of formed stars, and r is the size of the star cluster. Cluster member stars are scattered into the loss cone orbit with the time scale of t_{relax} and falls onto the central BH. If the central object is a BH binary instead, then a part of the accreted star will be ejected. If we assume all the accreted star

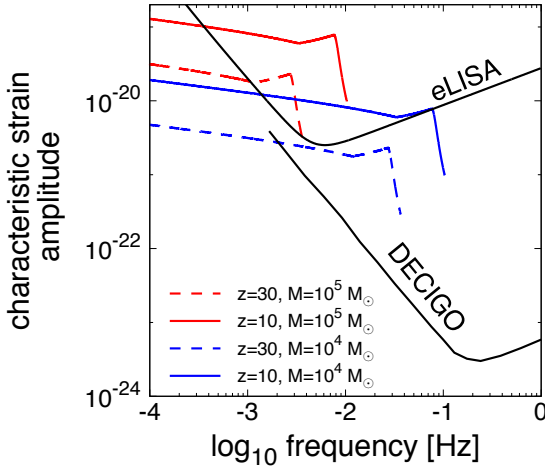


Figure 18. Characteristic strain amplitudes for merging BH-BH binaries against noise amplitudes of the future observational facilities. Only the equal-mass binaries with $10^4 M_\odot$ BHs (blue) and $10^5 M_\odot$ BHs (red) are considered. For each case, the solid and dashed lines represent the merger events occurring at $z = 10$ and 30 . The black solid lines show the expected noise amplitudes of eLISA (Amaro-Seoane et al. 2012) and DECIGO (Kawamura et al. 2011)

ejected at a speed of the escape velocity $v_{\text{esc}} = \sqrt{GM_{\text{BH}}/a}$, then the angular momentum loss with time $t_{\text{star,merge}}$ is

$$t_{\text{star,merge}} \sim \frac{J}{\langle M_* \rangle v_{\text{esc}} a / t_{\text{relax}}} \sim \frac{M_{\text{BH}}}{\langle M_* \rangle} t_{\text{relax}} \\ \sim 1.6 \times 10^7 \text{ yr} \left(\frac{10^3 M_\odot}{\langle M_* \rangle} \right)^2 \left(\frac{M_{\text{BH}}}{10^5 M_\odot} \right)^2 \left(\frac{100 \text{ AU}}{a} \right). \quad (18)$$

Thus, the BH binary separation can decrease through interaction with the stars formed in the same cloud.

After the formation of the DCBH, the host cloud will merge with the nearby massive galaxy (the LW radiation source). The stellar mass of the source galaxy is 10^6 and $10^7 M_\odot$ for the filamentary and the spherical clouds, respectively. The mass of the cold gas within the source galaxy is an order of magnitude larger than the stellar mass. The BH binary is likely to shrink by interacting with the cold gas and stars inside the source galaxy, and will finally merge due to gravitational wave emission.

The amplitudes of the gravitational waves from merging DCBHs peak at the frequency of 1–10 mHz at the rest frame. Thus the ground based GW detectors are difficult to detect the GWs. The space GW detectors such as evolved Laser Interferometer Space Antenna (eLISA) and Deci-hertz Interferometer Gravitational wave Observatory (DECIGO) can target these GWs.

Fig. 18 shows the characteristic strain amplitude $h_c(f)$ for binaries at $z = 10$ (solid) and 30 (dashed). The waveforms are calculated following the template given by Ajith et al. (2011). We assume equal mass binaries, where the mass of each BH is 10^4 (blue) and $10^5 M_\odot$ (red). Black solid lines show the noise amplitudes of eLISA and DECIGO. Binaries with 10^4 – $10^5 M_\odot$ can be observed at $z \gtrsim 10$. If the seed BH of the observed SMBHs are provided by the DC model,

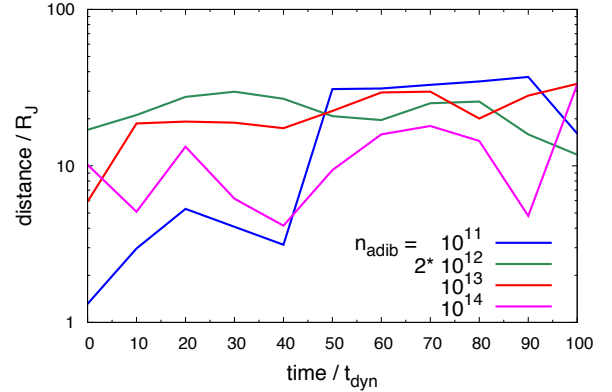


Figure 19. Time evolutions of the separation between the most massive protostar and the closest one with different threshold number densities n_{adib} , above which the gas is assumed to evolve adiabatically. The time is measured in the unit of the free-fall time with the threshold density n_{adib} for each case. The separation is normalized by the Jeans length with the same threshold density and the fixed temperature $T = 8000$ K. The time origin corresponds to the moment when the closest protostar is formed in the disk.

we expect a large number of BH binaries with 10^4 – $10^5 M_\odot$ at $z > 6$. Although the exact number density of DCBHs is under debate, detection of gravitational waves from DCBH binaries in this mass range will place important constraints on the formation scenario of SMBHs.

5.3 Effect of FUV self-shielding on the disk structure

Since we do not include H_2 self-shielding against the external LW radiation in this study, we may overestimate the photodissociation rate. To see whether the shielding effect can modify the disk structure with some enhanced H_2 abundance, we have performed following test simulations; for simplicity, we completely omit the LW field when the gas density exceeds $n_{\text{crit}} = 10^6 \text{ cm}^{-3}$, where the cloud becomes optically thick to the external LW radiation (Draine & Bertoldi 1996). We have continued to follow the evolution in the accretion stage for 2000 years.

As a result, we find almost no differences between the simulations with and without the external LW field. Even without the LW field, H_2 is completely destroyed within the disk, typically only with the H_2 abundance of $\sim 10^{-8}$. The atomic hydrogen cooling still dominates the molecular cooling. Some regions are cooled by adiabatic expansion to have ~ 3000 K, but it is also seen in the default cases with the LW field. We thus conclude that the presence of the LW field has almost no impacts on the disk structure. Our ignorance of the FUV self-shielding has no effects either.

In fact, H_2 molecules are mainly destroyed by collisional dissociation, not by photodissociation with LW photons. Inayoshi & Omukai (2012) show that it occurs in the thermal state characterized by $n \gtrsim 10^4 \text{ cm}^{-3}$ and $T \gtrsim 5000$ K. In our simulations, most part of the disk really satisfies the condition for the collision to dominate the dissociation.

5.4 Numerical resolution

In our study, the spatial resolution is limited by the adiabatic threshold density n_{adib} , above which the gas is forced to behave adiabatically with $\gamma = 5/3$. In reality, the threshold density is physically determined as $n_{\text{adib}} \simeq 10^{16} \text{ cm}^{-3}$ (Omukai 2001). The reason why we use the lower value $n_{\text{adib}} = 10^{13} \text{ cm}^{-3}$ is to save computational costs to follow the long-term evolution. To see how such an artificial EOS affects our results, we run test simulations with changing the threshold density.

The test simulations follow the evolution in the accretion stage where the disk fragmentation occurs in the filamentary cloud. In particular, we focus on the evolution of the orbital separation R_{sep} between the most massive protostar and another one close to it. Fig. 19 shows the time evolution of R_{sep} with different thresholds $n_{\text{adib}} = 10^{11}$ (blue), 2×10^{12} (green), 10^{13} (red), and 10^{14} cm^{-3} (magenta). We here normalize the time by the dynamical time t_{dyn} and the separation by the Jeans length R_J assuming a fixed temperature of 8000 K,

$$t_{\text{dyn}} = 27 \text{ yr} \left(\frac{n_{\text{adib}}}{10^{13} \text{ cm}^{-3}} \right)^{-1/2}, \quad (19)$$

$$R_J = 44 \text{ AU} \left(\frac{n_{\text{adib}}}{10^{13} \text{ cm}^{-3}} \right)^{-1/2} \left(\frac{T}{8000 \text{ K}} \right)^{1/2}. \quad (20)$$

In all the examined cases, the disk violently fragments into many pieces in an early stage of $t \lesssim 50 t_{\text{dyn}}$. Some protostars migrate inward to merge with the central star, whereas others remain in stable orbits. Fig. 19 shows that the separation converges to a few ten times R_J after $\simeq 50 t_{\text{dyn}}$ in all the cases. This suggests that more tighter binaries will be resolved with the higher threshold density, with which the Jeans length is smaller and resulting resolution is higher (Machida & Doi 2013).

In our cases, however, recall that the radius of a rapidly accreting protostar with $\sim 10^3 M_{\odot}$ is $\simeq 40 \text{ AU}$ (see eq. 3) and tight binaries with the smaller separations are assumed to be merged. The Jeans length with the default threshold density $n_{\text{adib}} = 10^{13} \text{ cm}^{-3}$ is $R_J \simeq 40 \text{ AU}$, comparable to the radius of the bloated protostars. Binaries with the smaller separations will appear with the higher threshold, but in any rate they will be merged away after the stars grow in mass and greatly inflate. We thus conclude that our choice of somewhat low threshold density will only have a limited effect on our conclusions. It is to be confirmed by future simulations with substantially higher spatial resolutions.

6 SUMMARY

We have studied long-term ($\sim 0.1 \text{ Myr}$) evolution through the accretion phase of SMS formation by performing 3D radiation-hydrodynamic simulations. We argue that tidal force of nearby galaxies plays a critical role. As shown by Chon et al. (2016), first of all, the cloud collapse is actually prevented by this effect in many cases. In this paper, we show that the tidal force still dominates the later evolution for the rare cases where the cloud collapses. In our simulation, one cloud is distorted by the strong tidal force of a nearby massive galaxy, and is deformed to be a filament. Fragmentation yields multiple star-disk systems, and further

fragmentation occurs in each disk, and more than 10 stars with a few $\times 10^3 M_{\odot}$ are finally formed. In the other case, the gas cloud collapses almost spherically with a relatively weak tidal field. Only a single star-disk system forms in this case, and a few stars are formed within the disk. The stellar masses at 0.1 Myr are $\sim \text{a few} \times 10^4 M_{\odot}$ in this case, but the stars are still accreting at a high rate of $0.1 M_{\odot} \text{ yr}^{-1}$. They are likely to evolve into the SMSs with $\sim 10^5 M_{\odot}$ before the end of their lives.

Throughout our simulations, the UV feedback plays a minor role. There are two reasons for this. Firstly, the accretion rate onto a protostar is still as large as $\sim 0.1 M_{\odot} \text{ yr}^{-1}$, even in the case where the surrounding gas is accreted onto multiple protostars. The protostars are in the supergiant stage with having a cool atmosphere ($T_{\text{eff}} \simeq 5000 \text{ K}$). The resulting UV emissivity is not strong enough to ionize the surrounding gas. Secondly, even if the gas is ionized, the effect of the UV feedback is actually limited. The H II region remains small and is trapped within the accretion flow. Since such an H II region cannot dynamically expand, the accretion is not halted. According to our analytic estimates, an H II region begins to dynamically break through the accretion envelope only after the stellar mass exceeds $\sim 10^5 M_{\odot}$.

The accreting SMSs in our simulations are expected to collapse into massive BHs at the end of their lives (Umeda et al. 2016). We thus suggest that 10^4 – $10^5 M_{\odot}$ BHs are formed sufficiently early at $z = 18 - 12$. Since these BHs will merge into the nearby massive galaxy and sink toward the galaxy center, they will experience large amount of mass accretion. If efficient accretion with nearly the Eddington rate lasts until $z \sim 7$, they can attain masses greater than $3 \times 10^8 M_{\odot}$ by $z = 7$. Whether radiation from the BH accretion disk prevents the efficient mass accretion is unclear, and hence warrants further study.

We also find that binaries of 10^4 – $10^5 M_{\odot}$ SMSs (and hence BHs) are formed in both the filamentary and the spherical clouds. These binaries will coalesce and emit a huge amount of GWs, which can be detected by the future space observatories, eLISA and DECIGO. Such future GW detection will provide us a valuable opportunity to understand the formation of early SMBHs.

We thank G. Chiaki, H. Susa, K. Omukai and S. Hirano for fruitful discussions and comments. This work is financially supported by Advanced Leading Graduate Course for Photon Science program, by Grant-in-Aid for JSPS Fellows (16J07507: S.C.), and by the Grants-in-Aid for Basic Research by the Ministry of Education, Science and Culture of Japan (15H00776, 16H05996, 17H06360: T.H.; 25287050: N.Y.). Numerical computations are carried out on XC30 at the Center for Computational Astrophysics (CfCA) of the National Astronomical Observatory of Japan. We use the SPH visualization tool SPLASH (Price 2007) in Figs. 1, 4, 7, 8, 14, and 16.

REFERENCES

- Abbott B. P., et al., 2016, *Physical Review Letters*, **116**, 241102
 Abel T., Norman M. L., Madau P., 1999, *ApJ*, **523**, 66

- Agarwal B., Khochfar S., Johnson J. L., Neistein E., Dalla Vecchia C., Livio M., 2012, *MNRAS*, **425**, 2854
- Ajith P., et al., 2011, *Physical Review Letters*, **106**, 241101
- Amaro-Seoane P., et al., 2012, *Classical and Quantum Gravity*, **29**, 124016
- Bate M. R., Bonnell I. A., Price N. M., 1995, *MNRAS*, **277**, 362
- Becerra F., Greif T. H., Springel V., Hernquist L. E., 2015, *MNRAS*, **446**, 2380
- Bromm V., Loeb A., 2003, *ApJ*, **596**, 34
- Casares J., Jonker P. G., 2014, *Space Sci. Rev.*, **183**, 223
- Chiaki G., Yoshida N., Hirano S., 2016, *MNRAS*, **463**, 2781
- Choi J.-H., Shlosman I., Begelman M. C., 2015, *MNRAS*, **450**, 4411
- Chon S., Latif M. A., 2017, *MNRAS*, **467**, 4293
- Chon S., Hirano S., Hosokawa T., Yoshida N., 2016, *ApJ*, **832**, 134
- Di Matteo T., Khandai N., DeGraf C., Feng Y., Croft R. A. C., Lopez J., Springel V., 2012, *ApJ*, **745**, L29
- Dijkstra M., Ferrara A., Mesinger A., 2014, *MNRAS*, **442**, 2036
- Draine B. T., Bertoldi F., 1996, *ApJ*, **468**, 269
- Gammie C. F., 2001, *ApJ*, **553**, 174
- Greif T. H., Bromm V., Clark P. C., Glover S. C. O., Smith R. J., Klessen R. S., Yoshida N., Springel V., 2012, *MNRAS*, **424**, 399
- Habouzit M., Volonteri M., Latif M., Dubois Y., Peirani S., 2016, preprint, ([arXiv:1601.00557](https://arxiv.org/abs/1601.00557))
- Hanawa T., Matsumoto T., 2000, *PASJ*, **52**, 241
- Hayashi C., 1961, *PASJ*, **13**, 450
- Heger A., Fryer C. L., Woosley S. E., Langer N., Hartmann D. H., 2003, *ApJ*, **591**, 288
- Hirano S., Hosokawa T., Yoshida N., Umeda H., Omukai K., Chiaki G., Yorke H. W., 2014, *ApJ*, **781**, 60
- Hirano S., Hosokawa T., Yoshida N., Omukai K., Yorke H. W., 2015, *MNRAS*, **448**, 568
- Hirano S., Hosokawa T., Yoshida N., Kuiper R., 2017, *Science*, **357**, 1375
- Hosokawa T., Omukai K., Yoshida N., Yorke H. W., 2011, *Science*, **334**, 1250
- Hosokawa T., Omukai K., Yorke H. W., 2012, *ApJ*, **756**, 93
- Hosokawa T., Yorke H. W., Inayoshi K., Omukai K., Yoshida N., 2013, *ApJ*, **778**, 178
- Hosokawa T., Hirano S., Kuiper R., Yorke H. W., Omukai K., Yoshida N., 2016, *ApJ*, **824**, 119
- Hubber D. A., Walch S., Whitworth A. P., 2013, *MNRAS*, **430**, 3261
- Inayoshi K., Omukai K., 2012, *MNRAS*, **422**, 2539
- Inayoshi K., Omukai K., Tasker E., 2014, *MNRAS*, **445**, L109
- Kashiyama K., Inayoshi K., 2016, *ApJ*, **826**, 80
- Kawamura S., et al., 2011, *Classical and Quantum Gravity*, **28**, 094011
- Kessel-Deynet O., Burkert A., 2000, *MNRAS*, **315**, 713
- Kitsionas S., Whitworth A. P., 2002, *MNRAS*, **330**, 129
- Larson R. B., 1969, *MNRAS*, **145**, 271
- Latif M. A., Schleicher D. R. G., Schmidt W., Niemeyer J. C., 2013, *MNRAS*, **436**, 2989
- Latif M. A., Bovino S., Van Borm C., Grassi T., Schleicher D. R. G., Spaans M., 2014, *MNRAS*, **443**, 1979
- Li Y., et al., 2007, *ApJ*, **665**, 187
- Machida M. N., Doi K., 2013, *MNRAS*, **435**, 3283
- McKee C. F., Tan J. C., 2008, *ApJ*, **681**, 771
- Milosavljević M., Bromm V., Couch S. M., Oh S. P., 2009, *ApJ*, **698**, 766
- Mortlock D. J., et al., 2011, *Nature*, **474**, 616
- Nelson A. F., 2006, *MNRAS*, **373**, 1039
- Omukai K., 2001, *ApJ*, **546**, 635
- Omukai K., Inutsuka S.-i., 2002, *MNRAS*, **332**, 59
- Park K., Ricotti M., 2011, *ApJ*, **739**, 2
- Peters P. C., 1964, *Phys. Rev.*, **136**, B1224
- Price D. J., 2007, *Publ. Astron. Soc. Australia*, **24**, 159
- Regan J. A., Haehnelt M. G., 2009, *MNRAS*, **396**, 343
- Regan J. A., Visbal E., Wise J. H., Haiman Z., Johansson P. H., Bryan G. L., 2017, *Nature Astronomy*, **1**, 0075
- Rybicki G. B., Lightman A. P., 1979, *Radiative processes in astrophysics*
- Sakurai Y., Hosokawa T., Yoshida N., Yorke H. W., 2015, *MNRAS*, **452**, 755
- Sakurai Y., Vorobyov E. I., Hosokawa T., Yoshida N., Omukai K., Yorke H. W., 2016, *MNRAS*, **459**, 1137
- Schleicher D. R. G., Palla F., Ferrara A., Galli D., Latif M., 2013, *A&A*, **558**, A59
- Shang C., Bryan G. L., Haiman Z., 2010, *MNRAS*, **402**, 1249
- Shibata M., Shapiro S. L., 2002, *ApJ*, **572**, L39
- Shibata M., Sekiguchi Y., Uchida H., Umeda H., 2016, *Phys. Rev.*, **D94**, 021501
- Springel V., 2005, *MNRAS*, **364**, 1105
- Stacy A., Bromm V., Lee A. T., 2016, *MNRAS*, **462**, 1307
- Sugimura K., Omukai K., Inoue A. K., 2014, *MNRAS*, **445**, 544
- Susa H., 2006, *PASJ*, **58**, 445
- Susa H., Hasegawa K., Tominaga N., 2014, *ApJ*, **792**, 32
- Takahashi S. Z., Tsukamoto Y., Inutsuka S., 2016, *MNRAS*, **458**, 3597
- Truelove J. K., Klein R. I., McKee C. F., Holliman II J. H., Howell L. H., Greenough J. A., 1997, *ApJ*, **489**, L179
- Tsuribe T., Omukai K., 2006, *ApJ*, **642**, L61
- Uchida H., Shibata M., Yoshida T., Sekiguchi Y., Umeda H., 2017, preprint, ([arXiv:1704.00433](https://arxiv.org/abs/1704.00433))
- Umeda H., Hosokawa T., Omukai K., Yoshida N., 2016, *ApJ*, **830**, L34
- Venemans B. P., Walter F., Zschaechner L., Decarli R., De Rosa G., Findlay J. R., McMahon R. G., Sutherland W. J., 2016, *ApJ*, **816**, 37
- Visbal E., Haiman Z., Bryan G. L., 2014, *MNRAS*, **442**, L100
- Volonteri M., 2010, *A&ARv*, **18**, 279
- Vorobyov E. I., DeSouza A. L., Basu S., 2013, *ApJ*, **768**, 131
- Willott C. J., et al., 2010, *AJ*, **139**, 906
- Woods T. E., Heger A., Whalen D. J., Haemmerle L., Klessen R. S., 2017, preprint, ([arXiv:1703.07480](https://arxiv.org/abs/1703.07480))
- Wu X.-B., et al., 2015, *Nature*, **518**, 512
- Yoshida N., 2006, *New Astron. Rev.*, **50**, 19
- Yoshida N., Abel T., Hernquist L., Sugiyama N., 2003, *ApJ*, **592**, 645

APPENDIX A: ANALYTIC ESTIMATE OF THE RADIATION FEEDBACK EFFECTS

We here analytically investigate whether the ionizing radiation from the protostar evacuates the surrounding gas. We consider a central star associated with a gas disk. As shown in our simulations, a photoionized region first expands toward polar regions where the density is relatively low (Fig. 16). We first model the density profile along the polar axis by the following density profile,

$$n(r) = \begin{cases} \frac{c_{s,I}^2}{G\mu_I m_p} r^{-2} & (r > R_{B,I}), \\ \frac{c_{s,I}^2}{G\mu_I m_p} R_{B,I}^{-2} \left(\frac{r}{R_{B,I}}\right)^{-\alpha} & (r < R_{B,I}), \end{cases} \quad (\text{A1})$$

where $R_B \equiv GM_*/c_s^2$ is the gravitational radius, c_s the sound speed, and $1 < \alpha < 1.5$ a free-parameter to characterize the inner density profile. The physical quantities with subscripts I and II correspond to those in neutral and ionized regions. We have assumed that the density profile follows $n \propto r^{-2}$ in the outer region $r > R_{B,I}$ and it becomes shallower within $R_{B,I}$ because of the gravity of the central star (McKee & Tan 2008). The spherically collapsing cloud yields $\alpha = 1.5$, while α slightly decreases when the disk forms around the central star. In fact, our simulations suggest $1.1 \lesssim \alpha \lesssim 1.3$.

The Strömgren radius R_{St} , inside which the ionizing photon supply is fully consumed by the recombination, is calculated by solving

$$S_{UV} = \int_{R_*}^{R_{St}} 4\pi r^2 \alpha_B n(r)^2 dr, \quad (\text{A2})$$

where S_{UV} and R_* are the stellar UV emissivity and radius. With the density profiles given by eq. (A1), we obtain

$$R_{St} = \begin{cases} \left[\frac{(3-2\alpha)G^3\mu_I^2 m_p^2 M_*}{4\pi\alpha_B c_{s,I}^6} S_{UV} + \left(\frac{R_*}{R_{B,I}}\right)^{3-2\alpha} \right]^{1/(3-2\alpha)} R_{B,I} & (\alpha < 1.5), \\ R_* \exp\left(\frac{G^3\mu_I^2 m_p^2 M_*}{4\pi\alpha_B c_{s,I}^6} S_{UV}\right) & (\alpha = 1.5). \end{cases} \quad (\text{A3})$$

Note that the expression with $\alpha = 1.5$ coincides with that found in Omukai & Inutsuka (2002). We assume S_{UV} is equal to the Eddington luminosity, which is valid for very massive stars, and R_* as the ZAMS radius,

$$S_{UV} = 10^{49} \text{ s}^{-1} \left(\frac{M_*}{M_\odot}\right), \quad (\text{A4})$$

$$R_* = 4.24 R_\odot \left(\frac{M_*}{100 M_\odot}\right)^{0.59}. \quad (\text{A5})$$

To see whether the ionized gas is gravitationally bound, we compare the Strömgren radius to the gravitational radius of the ionized gas. For $\alpha < 1.5$, we get

$$\begin{aligned} \frac{R_{St}}{R_{B,II}} &= \left(\frac{c_{s,II}}{c_{s,I}}\right)^2 \left[\frac{(3-2\alpha)G^3\mu_I^2 m_p^2 S_{UV} M_*}{4\pi\alpha_B c_{s,I}^6} \right]^{1/(3-2\alpha)} \\ &= 3 \left[4.4 \times 10^{-5} (3-2\alpha) \left(\frac{M_*}{10^3 M_\odot}\right)^2 \right]^{1/(3-2\alpha)}, \end{aligned} \quad (\text{A6})$$

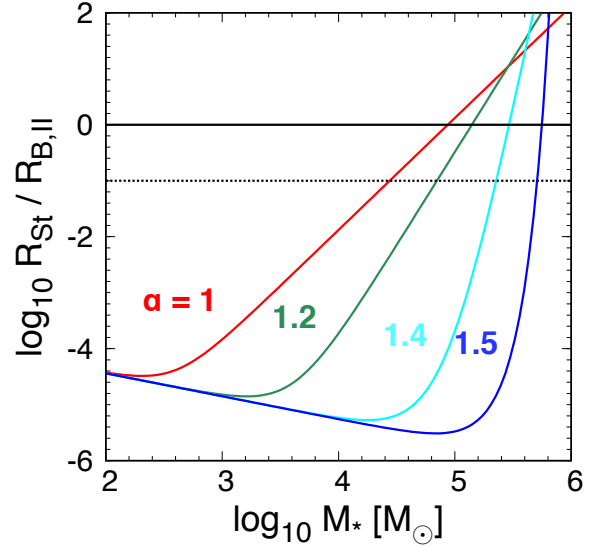


Figure A1. Ratios of the Strömgren radius R_{St} (eq. A3) to gravitational radius of the ionized gas $R_{B,II}$ as a function of the mass of the central star. The red, green, cyan, and blue lines represent the different density profiles within the gravitational radius (eq. A1) with $\alpha = 1, 1.2, 1.4$, and 1.5 . The horizontal solid line is a critical line of $R_{st} = R_{B,II}$, above which a photoionized region extends beyond the gravitational radius. The horizontal dotted line is also another critical line for the breakout of the ionized region $R_{st} = 0.1 R_{B,II}$, considering the effect of the radiation pressure against the gravity (see text).

where we have neglected the second term of eq. (A3). In the last equation, we assume $\mu_I = 1.2$, $\mu_{II} = 0.6$, $T_I = 8000$ K, and $T_{II} = 1.5 \times 10^4$ K, which are motivated by our simulation results.

Fig. A1 shows $R_{St}/R_{B,II}$ as a function of M_* for different α . For $1 < \alpha < 1.5$, the Strömgren radius exceeds the gravitational radius only for $M_* \gtrsim 10^5 M_\odot$. The ionized region is gravitationally bound and confined around the star until the stellar mass exceeds $\sim 10^5 M_\odot$. Such a trapped ionized region never disturbs the mass accretion. We thus reinforce our argument in Section 4, i.e., the UV feedback plays almost no roles in the evolution followed in our simulations.

We have neglected the effect of the radiation pressure in the above estimate. Thomson scattering effectively counteracts the gravity, so that it helps the expansion of the ionized region. Such an effect is included in our modeling with reducing $R_{B,II}$ by a factor of $\Gamma \equiv 1 - L/L_{\text{Edd}}(M_{\text{tot}})$, where L is the stellar luminosity, L_{Edd} the Eddington luminosity, and M_{tot} the total mass within the ionized region including the gas and star. Accordingly, the condition for the breakout of the ionized region is modified as $R_{St}/R_{B,II} = \Gamma$. The highest-mass stars that appear in our simulations have $\Gamma \sim 0.1$, but Fig. A1 still shows that the breakout occurs only for $M_* \gtrsim 10^4 M_\odot$. Therefore, our conclusions are not affected by this effect.